POWER CONSUMPTION IN PRESSURE SCREENS

by

YUBING LI

B.Eng., Shanghai Jiaotong University, 1991
M.Eng., Shanghai Jiaotong University, 1994

A THESIS SUBMITTED IN PATIAL FULFILMENT OF
THE REQUIREMENTS FOR THE DEGREE OF

MASTER OF APPLIED SCIENCE

in

THE FACULTY OF GRADUATE STUDIES
DEPARTMENT OF MECHANICAL ENGINEERING

We accept this thesis as conforming

to the required standard

THE UNIVERISTY OF BRITISH COLUMBIA
August 2003

Library Authorization

Yubing Li
Name of Author *(please print)*

24/02/2004
Date (dd/mm/yyyy)

Title of Thesis: Power consumption in pressure screens

Degree: M.A.Sc

Year: 2004

Department of Mechanical Engineering
The University of British Columbia
Vancouver, BC Canada

Abstract

Pressure screens are an important unit operation in the manufacture of high quality pulp and paper. During screening, a suspension of water, fibre and contaminants are separated based on their physical dimensions. Most of the research conducted previously focused on the fibre separation or contaminant separation performance, with few studies available in the field of power consumption. The objective of this dissertation is to investigate the factors that influence the power consumption in a pressure screen. This was accomplished by experimentally measuring the torque exerted on the rotor shaft in a laboratory Cross Sectional Screen for a wide range of design and operating conditions. The experimental results are presented in non-dimensional form and empirical correlations are derived.

Two conditions were considered in this thesis: a rotor without elements on its periphery (a smooth rotor) and a rotor with elements. It was found that for smooth rotors, the spacing between the rotor and outer housing had a relatively small influence on the required torque (power). The fluid type and viscosity affected the flow behavior in different ways. "Drag reduction" was observed for pulp suspensions. The non-dimensional torque, scaled using viscosity, could be expressed as a power-law function of Reynolds number. The value of the exponent in our experiments was in the range of 1.32 to 1.68.

For a rotor with elements, the additional torque generated by the elements was significantly influenced by the element height. This resulted from the high pressure drag on the leading edge of the elements and the vortices downstream. The torque coefficient based on the extra toque was independent of the Reynolds number, but was a strong function of the ratio of element height with rotor spacing.

Table of Contents

List of Tables

List of Figures

Acknowledgement

To Jianzhong

For all his love and constant support

I would like to extend my sincere thanks to my supervisors, James Olson and Mark Martinez, for their helpful guidance and encouragement. I appreciate the help from my colleague, Chuntao, Cameron, Edmond, Monica and Satya. There are many other people who deserve acknowledgement: Tim Patterson, Brenda Dutka, Lisa Brandley, Ken Wong, Doug Yueng, Glen Jolly, Dave Camp, Len Drakes, and Perry Yabuno. Thank you for those valuable assistance on this project.

A special thank for my parents for their unconditional love and support. Thank you, Annie, your laughter is my best inspiration.

This study was made possible by financial support from Advance Fiber Technologies (AFT), Pulp and Paper Research Institute of Canada (Paprican) and Natural Sciences Engineering Research Council (NSERC).

Chapter 1 Introduction

Screening is a technology in which suspensions of water, individual fibres and debris are separated based upon the physical properties of the particles. Screens, to remove un-pulped bits of wood (shives) and other contaminants, have always been an integral part of the pulping, paper-recycling and papermaking process.

The development of pulp screening technology has had three significant stages: Vibratory Flat Screens, Cowan Screens and Pressure Screens. Today, pressure screens are the most commonly employed equipment for contaminant removal and fibre fractionation. Contaminants reduce the strength and smoothness of the paper, and causes damage to the processing equipment. As an example, shives reduce the strength of paper as they hinder water fibre bonding and create voids in the paper. Voids lead to stress concentrations that may induce breakage during applications where high tensile forces are applied i.e. printing. Similarly, during chemical pulping, shives removal is beneficial as it leads to a reduction in bleaching chemicals.

Another application of screening is fiber fractionation which is the separation of fibres by their geometry. Fibre fractionation and the subsequent processing of the targeted fractions is an efficient means of producing high quality pulp. This has been demonstrated with both TMP and recycled fibres [1-4].

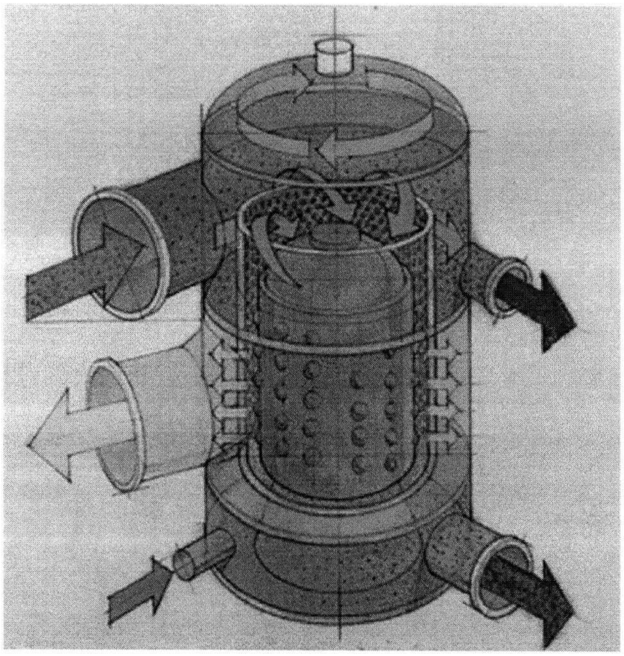

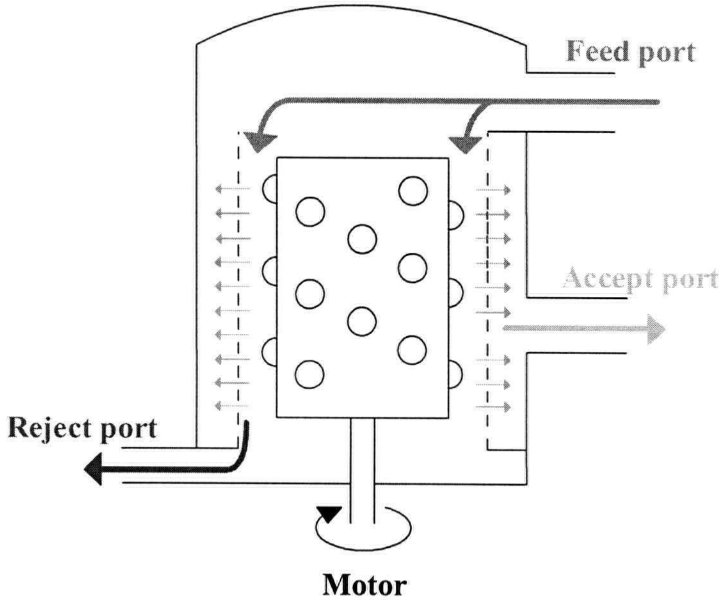

Figure 1.1: A typical pressure screen

Screens usually operate with a flow rate in excess of 10000 l/min and at a relatively low consistency, namely 1- 4%. Although screening at medium consistency (8-15%) has been investigated, it has yet to be applied industrially [5].

The two essential components in a pressure screen are a cylindrical screening basket and a rotor as shown in Figure 1.1. The pulp suspension enters the screen through the feed port and first passes over the rock trap, which prevents large debris from entering and damaging the screen plate and rotor. The pulp then flows down between the screen plate and the rotor. Fibres preferentially pass through the screen plate and out through the accept port, while the remaining pulp and contaminants are expressed through the reject port. With fractionation screening, the short fibers preferentially pass through the screen plate while the long fibres are retained. Dilution water near the reject area is necessary for preventing the highly thickened reject flow from plugging the pipe. The rotor produces both positive and negative pressure pulses to force fibers through the apertures and prevent the apertures from plugging.

Multiple stages of screens are used to concentrate the contaminants. A cascade-feedback arrangement is typically used where the reject stream from the first screen, with a high debris concentration, forms the feed to the secondary screen and the secondary screen's accept stream is recirculated to the feed of the first (Primary) screen. There are, however, numerous other configurations and these depend on the end needs of the user.

Screen performance is measured in terms of its throughput capacity (mass flow rate of the accept stream), its efficiency for removing contaminants, and its power consumption. There has been considerable work to improve the efficiency and capacity of the screens but there has been little work to improve and understand the power consumed during screening. With the increasing cost of electrical power, understanding and reducing power consumption is increasingly important. As a result, the main purpose of this research is to investigate the factors that influence the power consumption of pressure screens, such as rotor geometry (rotor diameter, the clearance between the rotor and the screen plate, element height etc.), and operating variables (pulp consistency and rotor speed).

Chapter 2 Literature Review

An overview of the properties of pulp suspensions, the components of pressure screens, and the variables and mechanisms that influence the performance of pressure screens is given below.

2.1 Rheology of pulp suspensions

2.1.1 Background

Newtonian fluids are those in which the property that the shear stress τ is proportional to the shear rate $\dot{\gamma}$ (or velocity gradient du/dy). The constant of proportionality is the dynamic viscosity of the fluid μ, i.e.

$$\tau = \mu \frac{du}{dy} = \mu \dot{\gamma} \tag{2.1}$$

Non-Newtonian fluids differ from Newtonian fluids in that the relationship between the shear stress and the flow field is more complicated. Examples include various suspensions such as coal-water or fiber-water slurries, food products, inks, glues, soaps, polymers solutions, etc. In general, non-Newtonian fluids are separated into various categories of purely viscous time-independent or time-dependent fluids and visco-elastic fluids [6]. Purely viscous time-dependent or time independent fluids are those in which the shear stress is only a function of the shear rate, but not in a linear manner. Visco-elastic fluids possess both viscous and elastic properties (as well as memory) and have received considerable attention because of their ability to reduce both drag and heat transfer in channel flows.

Figure 2.1 illustrates the characteristics of purely viscous time-independent fluids. In this case, fluid (a) is called pseudoplastic (or shear thinning), fluid (b) is dilatant (or shear thickening), fluid (c) is a Bingham plastic, and fluid (d), id defined as Hershel-Buckley fluid. A Newtonian fluid is depicted by (e).

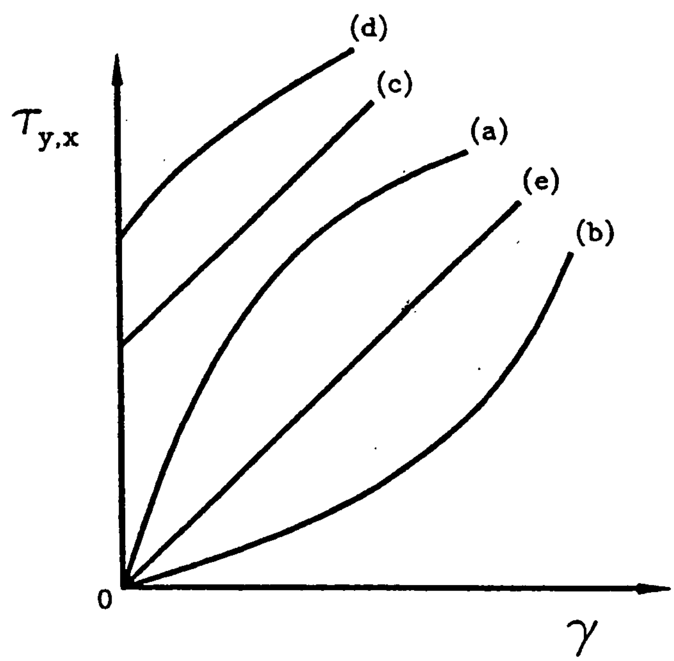

Figure 2.1: Flow curves of purely viscous, time-independent fluids: (a) pseudoplastic; (b) dilatant; (c) Bingham-plastic; (d) Hershel-Buckley; (e) Newtonian.[6]

2.1.2 Flow regimes

Three flow regimes have been observed for pulp suspensions in large diameter pipes: plug flow, mixed flow and turbulent flow, as presented in Figure 2.2. At low velocity, the fibre network flows as a plug, with fibres scraping along the wall. As velocity increases, fibres migrate away from the wall creating a clear water annulus between the plug and the wall. At the transition point, the annulus turns turbulent and the fluid stresses are sufficient to disrupt the surface of the plug, mixing fibres into the annulus. The size of the turbulent annulus increases and the plug decreases as the velocity increases. Eventually, the flow becomes turbulent, and the plug disappears.

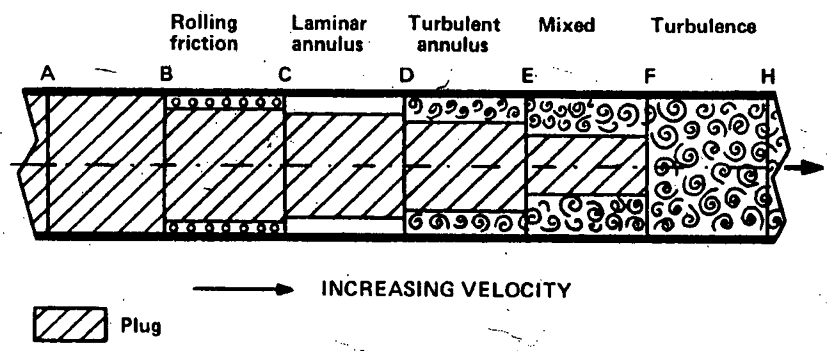

Figure 2.2 Illustration of various flow regimes of pulp suspension in a round pipe [14]

The flow regimes in a rotary device are different from that in a pipe. Bennington et al. [7] described flow regimes in a concentric cylinder device with an inner rotor (shown in Figure 2.3). Below the yield point, the pulp had been compressed and gas pockets have appeared behind the rotor lugs (a). After motion was initiated, Couette flow develops in a region bounded by stagnant pulp and flocs in the immediate rotor vicinity moved in a rolling tumbling manner (b). As the rotor speed was increased, this fluid–like zone increased in volume radically outward from the rotor to fill the entire housing (c). When the flow reached the outer housing wall, an abrupt transition in flow occurred. At low mass concentration, ($0.01 \le C_m \le 0.04$), outward radial flow developed (d) followed by a second transition to cellular flow characterized by inward radial motion displaying six-fold symmetry produced by the housing baffles (e). When $C_m \ge 0.04$ transition directly to the cellular flow pattern was observed (e). If the gas content of the suspension was sufficient to fill the volume between the rotor lugs, flow development could cease before the transition to cellular flow (f). If the air content was greater than that which could be accommodated by the rotor, the rotor simply rotated in the gas phase unable to transfer momentum to the suspension. The suspension could then cease movement completely (g).

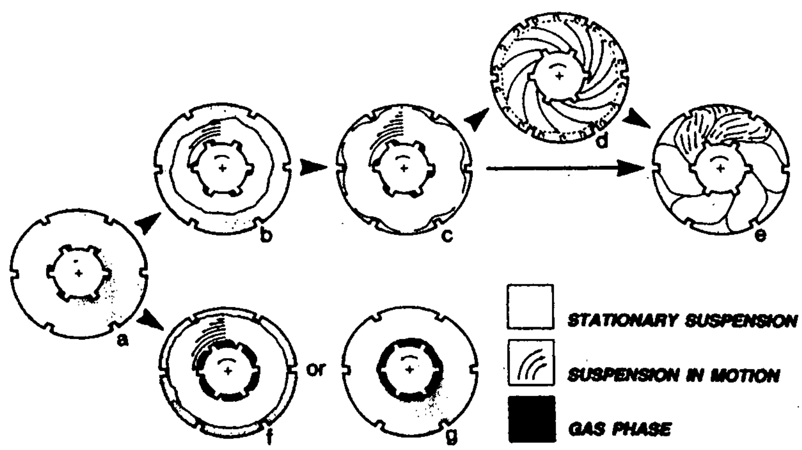

Figure 2.3: Flow regimes of semi-bleached Kraft suspension behavior in the wide-gap configuration observed from the front face of the shear tester [7]

2.1.3 Yield stress

A characteristic of fiber systems is their ability to form networks. Fiber networks develop mechanical strength from frictional forces at fiber contact points. This inhibits relative motion [8]. Only when the external forces exceed the yield stress, the suspension starts to flow and adopt some of the properties of a fluid [9].

Measuring the yield stress of a pulp suspension is complicated. First, the suspension is not uniform because it is flocculated. The strong network strength inside the fibre flocs will result in relative motion among flocs rather than among individual fibres. In addition, in some cases, the pulp suspension could not be considered as a continuum due to the relatively large size of the fibre flocs to the container geometry. An example is flow into narrow apertures which must be considered as a heterogeneous two-phase system [10].

One way to measure the yield stress of pulp suspension is using a concentric cylinder with a profiled rotor [11,12,13]. This device was first introduced by Gullichsen and Harkonen to measure the plug disruptive shear stress of pulp suspensions [14]. Other ways include stress rheometer [15].

For pulp fibre suspensions, the yield stress has typically been correlated with the suspension mass concentration using equation of the form:

$$\tau_y = aC_m^b \tag{2.2}$$

where C_m is the mass concentration of pulp suspension, a and b are constants depending on the test procedure employed, the pulp type and the degree of pulp treatment prior to testing. The average value of a is between 1.18 and 24.5, and b is between 1.25 and 3.02 when C_m is given as a percentage [8]. However, it was found that the relationship between the yield stress and mass concentration has a large deviation when the mass concentration increases into the medium consistency range due to the increasing quantity of air in the suspension [11]. So, the volumetric concentration is more powerful in correlating with suspension yield stress. Bennington et al [11] offered the correlations for several different types of pulps:

$$\text{SBK:} \quad \tau_y = 3.82 \times 10^5 C_v^{2.72} \tag{2.3}$$

$$\text{SGW:} \quad \tau_y = 1.08 \times 10^6 C_v^{3.36} \tag{2.4}$$

$$\text{TMP:} \quad \tau_y = 2.63 \times 10^6 C_v^{3.56} \tag{2.5}$$

where C_v is the volumetric concentration (%). Due to the different measuring techniques and pulp properties, Swerin [16] reported considerably lower values than the results from Bennington et al. Nevertheless, those equations are useful tools for estimating the shear levels required to cause pulp suspensions to flow.

While the yield stress depends primarily on the volume of the suspension occupied by the fibres, fiber physical properties also influence the yield stress. Wikström [17] investigated the effect from some process parameters and fiber characteristics. He concluded that the yield stress increased with increasing freeness, Kappa number and mean fiber length, while it decreased with increasing temperature and was fairly independent of pH. Moreover, he found that the fiber length distribution had a greater effect on the network strength than the mean fiber length.

2.1.4 Fluidization

The term fluidization, in the field of chemical engineering, is used to designate the gas-solid contacting process in which a bed of finely divided solids is lifted and agitated by a rising stream of process gas. The definition of "fluidization" in pulp suspension flow, however, remains somewhat arbitrary. In pipe flows, the fluidization refers to the turbulent flow regime because the level of shear required to rupture fibre networks can only be attained in the turbulent regime of flow. Therefore the terms fluidization and turbulence are almost synonymous in fibre suspensions. In the fluidized state, the pulp friction loss approaches that of water [18,19]. In rotary devices, however, there are two different opinions. Most of the researchers accept fluidization defined as the fluid-like motion created by exceeding the suspension yield stress and imposing sufficient shear to maintain fibre motion. In many cases, this occurs in only a part of the vessel, and therefore only a part of the suspension is fluidized. In contrast, Gullichsen et al. [14] and Harkonen [18] defined fluidization as the point where the entire pulp suspension becomes fully turbulent. This definition is similar to that in pipe flow, and they found the pulp suspension had the same flow properties as water in the fluidized state under the same conditions.

Fluidization implies relative motion among fibers which leads to energy dissipation. Thus energy dissipation becomes a useful means of quantifying fluidization. Wahren [20] was the first to employ the concept of "power dissipation per unit volume", ε, to quantify fluidization. He estimated values for the onset of fluidization by using yield stress of fiber network τ, and extending the expression of power dissipation in laminar flow. This gave:

$$\varepsilon_F = 1.2 \times 10^4 C_m^{5.3} \tag{2.6}$$

This theoretical estimate is two orders of magnitude higher than that measured by Gullichsen and Harkonen [14], and nearly three orders higher than the estimate given by Bennington and Kerekes [21]. The difference between results may be due to the different definition of fluidization and different pulp properties.

2.1.5 Apparent viscosity

Although a pulp suspension is an example of a non-Newtonian fluid and does not truly have the property of viscosity, it is convenient to define an apparent viscosity which is the ratio of the local shear stress to the shear rate at that point.

$$\mu_a = \frac{\tau}{\dot{\gamma}} \tag{2.7}$$

The apparent viscosity is not a true fluid property for non-Newtonian fluids because its value depends upon the flow field, or shear rate. The apparent viscosity of pulp suspension was given by [21]:

$$\mu_a = 1.5 \times 10^{-3} C_m^{3.1} \qquad 1 < C_m < 12.6\% \tag{2.8}$$

2.1.6 Drag reduction

The flow properties of pulp suspensions have a major influence on the pipe friction loss characteristics. This research was originated in the 1930's [22], and has subsequently been extended by other researchers [14,19]. An example, given in Figure 2.4, is frictional pressure loss for a sulfite pulp fiber suspension flowing through a large diameter, straight pipe. Fiber suspensions present a greater friction resistance than that of water at low velocities, and cross the water curve as the velocity increases. Newtonian behavior is then approached at higher velocities.

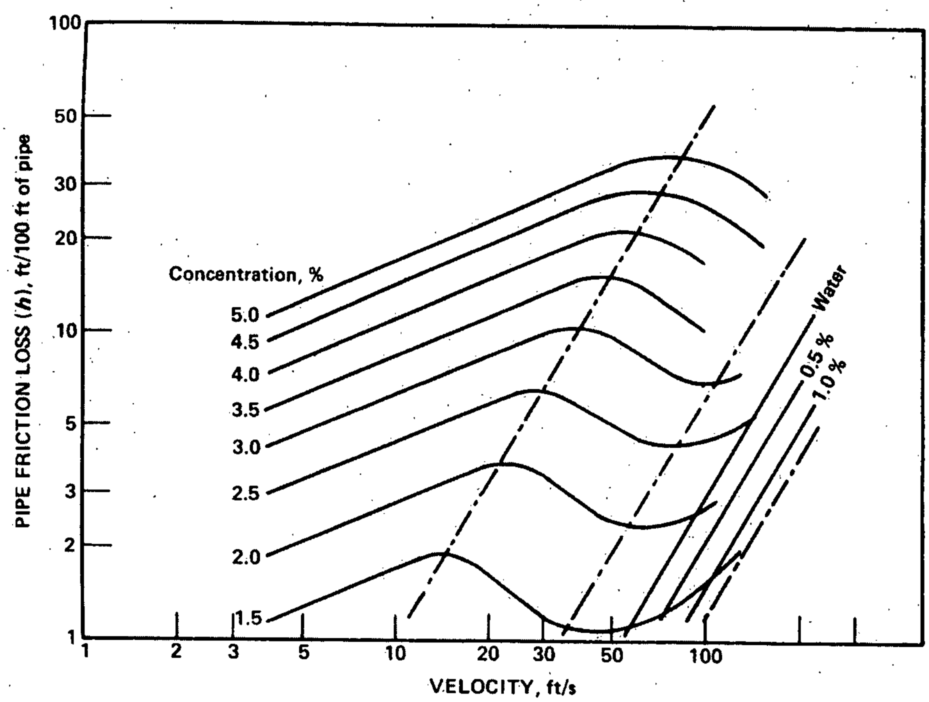

Figure 2.4 Friction loss vs. velocity for various consistencies of unbleached sulfite pulp [22].

The pressure drop can be expressed by shear stress and velocity as rate of shear (shown in Figure 2.5), and the curves in Figure 2.4 thus are presented in a more general form commonly used in non-Newtonian flow engineering. From the point where the fiber suspension and water flow curves, after crossing, become parallel, the whole suspension is assumed to be well-mixed or turbulent. The shear field imposed through the mass of fibers now exceeds the shear stress value, τ_d, needed to disrupt the fiber network completely.

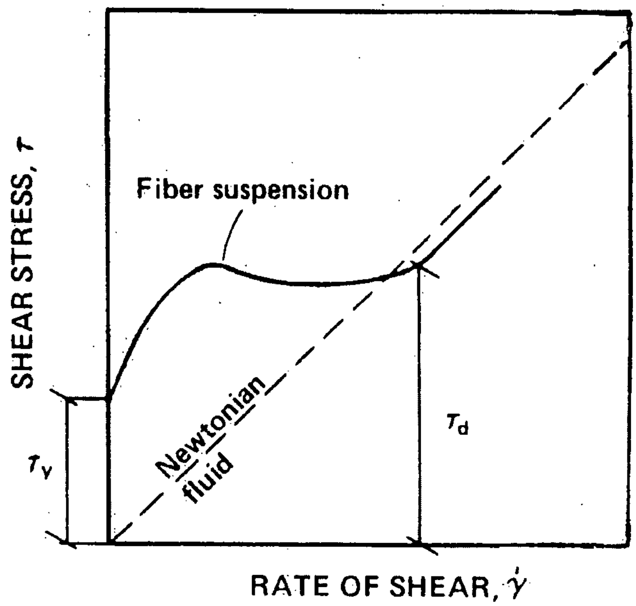

Figure 2.5: Shear –rate curve for a fiber suspension [14]

2.2 Pressure screening

2.2.1 Components

2.2.1.1 Screen basket

A wide variety of screen baskets have been developed for numerous applications and furnishes. There are two types of apertures used in the baskets, either holed or slotted; and the baskets may also be contoured on the feed side.

- **Holed baskets**

Traditional pressure screens are smooth, holed plates. The holes on the plates are typically manufactured by drilling. These baskets are easy to prepare and the cost is relatively low. In addition, the holed screen plates are more durable than the slotted plates and do not need to be replaced as often. At present, this type of screen plate is normally employed upstream of fine slotted screens in order to provide protection. They can also be used to effectively fractionate fibres by length.

For most recycled fiber applications, screen baskets have holes in the range of 0.050-0.079 inches (1.3-2.0 mm) and an open area in the range of 10-30%. Hole diameters are almost never below 1.0 mm.

- **Slotted baskets**

Most contaminant removal screening use slotted screen baskets. The slots are usually located at the right angles to the direction of the rotor. The slots are manufactured either by machining slots into metal or by joining wires together on a backing align to form very narrow slots. The slot width can be as small as 0.2 mm for softwood Kraft pulps and 0.15 mm for softwood TMP pulps. With a combination of holed and slotted screen baskets, it is possible to improve the efficiency of screening while greatly cutting down the energy consumption [23].

- **Smooth plates and contoured plates**

Both of the above two types of baskets have two kinds of surfaces, smooth surface (conventional) and contoured surface. The contoured baskets were first developed in Sweden in the 1970's and now are widely applied in pulping industry with different modifications [24,25,26]. Contours are depressions or protrusions on the feed side of the screen plates. Fundamental research has shown that contours can greatly reduce the hydraulic resistance of a screen plate by streamlining the flow through it [27,28]. Contours can also reduce accumulations of fibres in the slot by increasing the turbulence level at the entry and downstream of slots [28,30]. The biggest effect of the contours is that they can dramatically increase the screening capacity (mass flow rate through the cylinder). This allows significantly smaller slots to be used and, in turn, greatly improves the contaminant removal efficiency [25,28,32,33,34,35]. This capacity improvement resulted from the uneven surface which can disrupt and fluidize the boundary layer near the screen plate and align the pulp fibers to allow them to flow through the screen apertures. Furthermore, contoured cylinders can operate at considerably higher consistencies and are found to require less specific energy per ton of pulp [33]. However, contoured screen baskets are not suitable for fractionation since long fibres preferentially pass through the slots. Today, all industrial slotted screens use contours.

2.2.1.2 Rotors

Rotors play an important role in pressure screens. Their main purpose is to accelerate the pulp suspension to a high tangential velocity and to generate a pressure pulse that continuously backflushes the screen apertures. The cohesive forces between pulp fibers drive the fibers to form flocs very fast even at very low concentration [8]. The consequence of this is that the fibers will form cohesive structures at the surface of the screen cylinder which quickly leads to plugging. The rotor aids in preventing the screen from being plugged as the hydrofoils or bumps, will create negative pressure pulses that back-flush the pulp [31]. This was investigated by Karvinen and Halonen [36], with the action of the foiled type rotor by characterizedly using both experimental and computational techniques. It was found that the backflushing action of the pressure pulse arose from a Venturi effect created by the acceleration of the flow through the gap between the moving rotor tip and stationary screen plate. This acceleration causes the local pressure on the feed-side of the screen plate to decrease to the point that the flow through the aperture reverses. The flow then passed from the accept-side of the screen plate to the feed-side, releasing any plugged fibres. The magnitude of the pressure pulsation was affected by the foil shape, the rotational speed and the clearance between the foil and the screen plate. Stronger pulses (to remove more tightly held fibres) could be produced by either increasing the rotor speed or decreasing the size of the gap.

Rotors will not only clean the screen plate, but also improve the performance of screening. Rotors can create a high tangential fluid velocity at the surface of the screen plate, resulting in an increase in the screening efficiency [37]. Novel rotors introduce turbulence to the flow which greatly increases the capacity of screening [38].

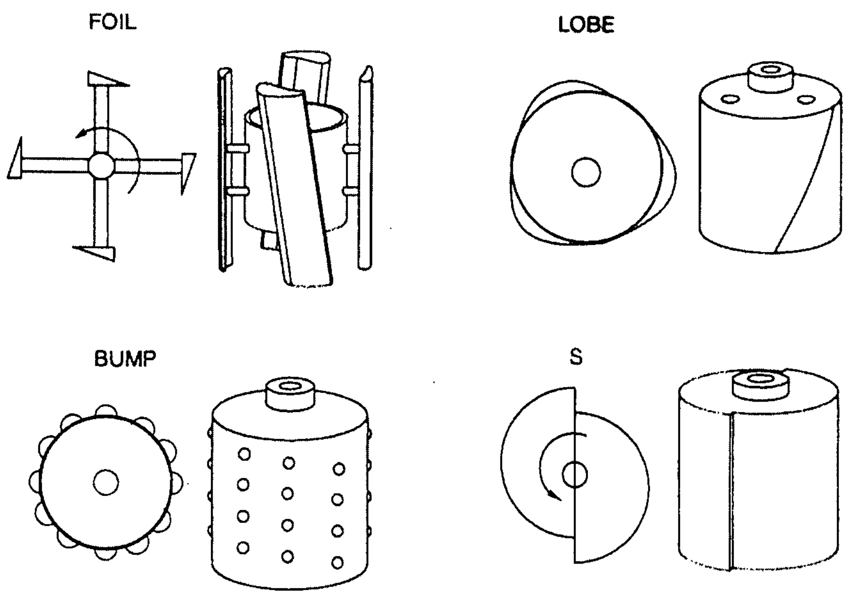

Figure 2.6: Rotor Types

In addition, the shape of the rotor body affects the screening results. A schematic of commercial rotors is shown in Figure 2.6. Compared to commonly employed cylindrical rotor, a conical rotor was found to be more advantageous because it ensures a uniform flow in the axial direction of the pressure screen [39].

2.2.2 Mechanism and Theory of pressure screening

2.2.2.1 Flow patterns

The mechanism that determines whether a fiber or a contaminant passes through the screen plate or be rejected is extremely complex. The fiber behavior at the feed-side surface, which is governed by the basket design, is the primary factor affecting throughput and efficiency [30]. Meanwhile, the fiber orientation and flow path are also affected by the rotor, the internal geometry and operation of the screen.

So far, there are many investigations available to study the flow pattern of the pulp near and through the screen apertures. Oosthuizen et al. [40] found that a highly curved flow field would be generated near a slot on the wall in a rectangular channel. Their experimental results confirmed that there was no significant separation of the flow on the upper wall, and the Reynolds number in their study (200~700) did not have a strong effect on the flow pattern. Gooding and Kerekes [41] filmed fiber trajectories in the entry zone of a single slot (0.5mm wide) in a 19-mm square channel. Two types of nylon fibers were of the same length (3.1mm) were used. In their experiment, .they observed that nearly all fibers, which passed into the slot, came from a thin layer adjacent to the wall upstream of the slot. They also observed that this "exit" layer is less concentrated than the main flow. Analysis of the films showed that screening took place by two mechanisms: a "wall effect" that lowered the concentration of stiff shive-like fibers in the flow entering the slot, and a "turning effect" that caused stiff shive-like fibers to rotate instead of bending as they turned into the slot. These rotating fibers tended to be swept away from the slot by the mainstream flow, whereas the more flexible pulp-like fibers tended to bend and enter the slot.

The different performance of smooth screen plates and contoured screen plates resulted from their different designs. The flow patterns at the feed-side surface of smooth and contoured screen baskets have been studied by Yu and DeFoe [29]. The wake length, the velocity profile inside the channel, and vortices were clearly observed in their experiments. The flow separation and vortices were observed on the contoured basket screen and there was no separation found on the surface of the smooth screen when flow went from feed side to accept side. Therefore, the conclusion was that the outward flow (accept flow) for the smooth basket was caused by local pressure difference only, while the outward flow for the contoured basket was mainly from reattachment of the flow stream. Halonen et al. [28] simulated flow patterns near a slot on a conventional and a contoured screen basket. They found that the flow fields on the contoured and conventional screen plate were quite different. The boundary layer of the contoured screen plate was significantly thicker than that of the conventional one. This was due to increased shear stresses on the screen plate surface. Additionally the shape caused the flow to bend more smoothly towards the slot, resulting in a uniform feed to the opening. Their study showed that at the same conditions, the average slot velocity for the contoured basket was about 50% higher than for the conventional basket. They also reported that the capacity of the slotted contoured basket was 50~300% greater than the conventional basket. These findings – that higher slot velocity implies greater capacity – agreed with those of Gooding and Kerekes [41]. However, Gooding also reported that higher slot velocities increased the probability that a shive would be accepted [42].

2.2.2.2 Pressure pulses

The negative pressure pulse generated by moving foils or bumps on the rotor periodically cleans the fibres in the apertures of the basket, allowing pressure screens to run continuously. The intermittent pulsing action is the essence of the pressure screening. The shape and magnitude of the pressure pulse is critical to the performance of pressure screens. With too small of a negative pulse, the rotor is not able to clean the slots, while too high of a pulse will lower the capacity of the screens as a large amount of material is backflushed [36]. Further, too high of a positive pulse may force deformable contaminants through the apertures. So in the design of a screen, the pressure pulsation ought to be minimized but still retain its cleaning effect.

The magnitude of the negative pressure pulse is a function of rotor type, rotational speed, and the clearance between the rotor and the screen. According to Yu [31], the pressure-pulse signature for a foil rotor and a contoured-drum rotor (s-rotor) are quite different, as seen in Figure 2.7. The lower rotational speed decreases both the frequency and the magnitude of the pulsation. Decreasing clearance between the rotor and basket significantly increases the peak-to-peak pressure pulse. A numerical method using turbulent $K-\varepsilon$ model was developed to simulate the pressure pulsation in pulp screens [36]. With this numerical model, it is possible to optimize design of pressure screens.

A: Pressure –pulse signature for a foil rotor

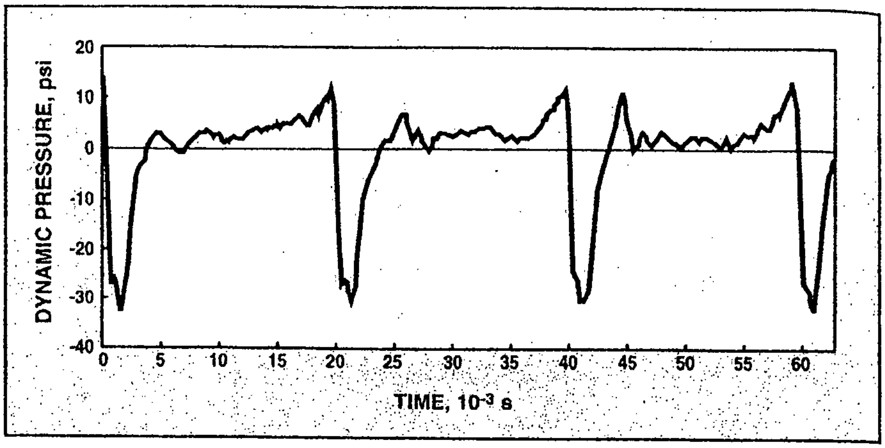

B: Pressure –pulse signature for a contoured-drum rotor

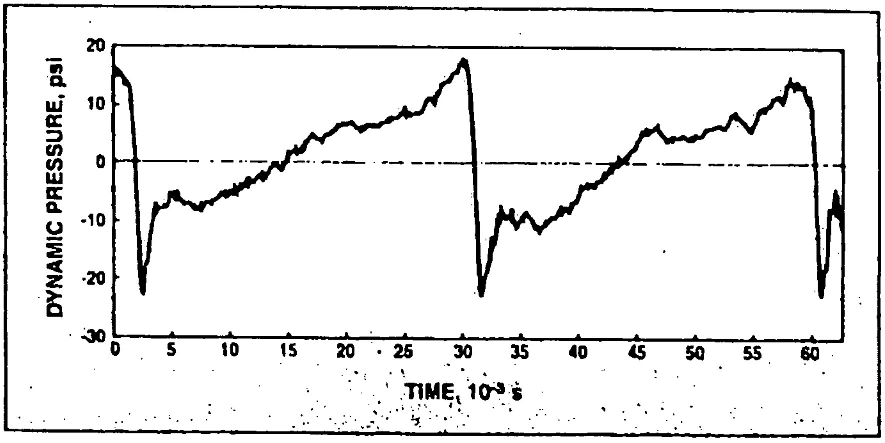

Figure 2.7: Different pressure-pulse signatures for different rotor shape [31]

More recently, Gonzalez [43] examined experimentally the pressure pulses produced by a NACA foil rotor running in a Cross Sectional Screen (CSS). It was shown that the magnitude of the pressure pulse was a complicated function of the foil shape, the angle of attack, the foil tip speed, the clearance between the foil with the screen plate, and the pulp consistency. Figure 2.8 showed the effect of gap (clearance) on the non-dimensional pressure pulsation in CSS. Feng [44] continued the study of pressure pulsation in CSS and developed a numerical method to calculate the pressure pulse generated in pressure screens by CFD simulation.

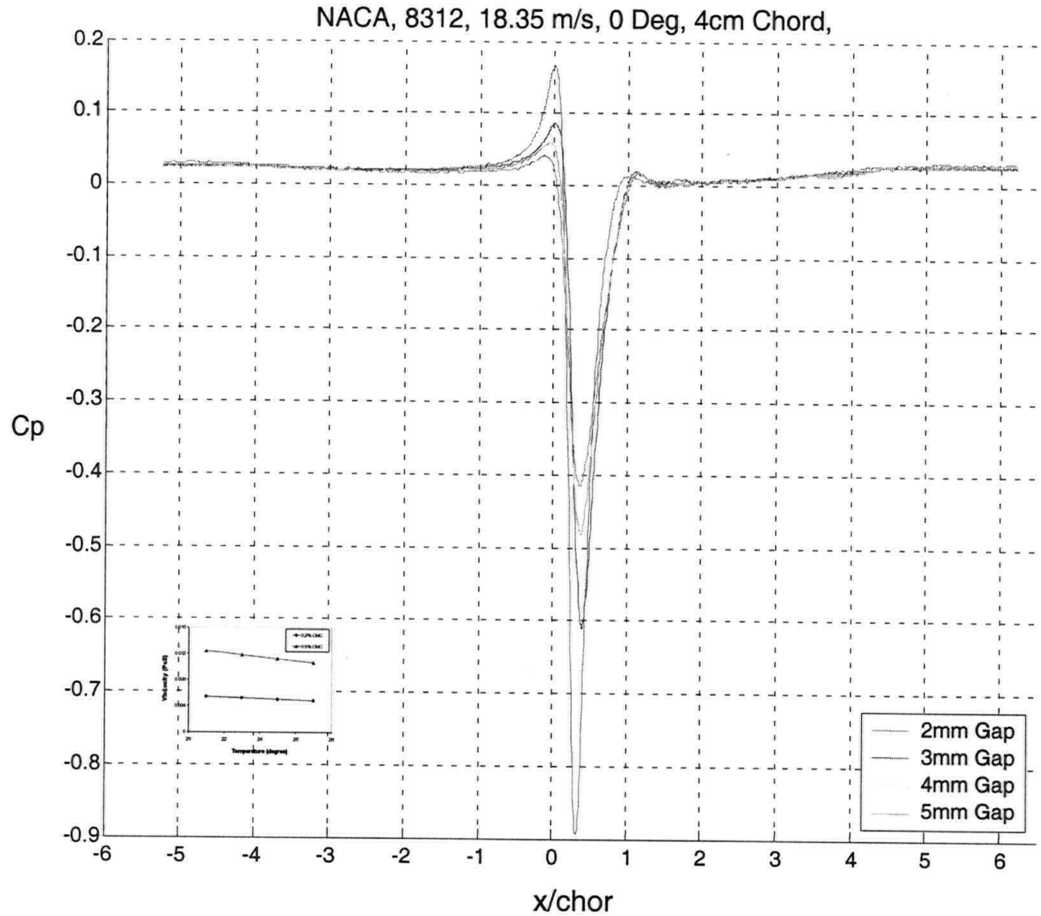

Figure 2.8: Collapsed Cp curves for different rotor clearances [43].

2.2.2.3 Passage ratio .

The extent to which fibers pass through individual apertures can be represented by a quantity called "passage ratio". Gooding and Kerekes [34] considered the passage ratio as a bulk quantity, which was defined as the ratio of the pulp consistency in the fluid passing through an aperture to the pulp consistency upstream of the aperture. Based on the bulk passage ratio, they developed a theoretical model that related consistency drop and reject thickening to reject ratio. Their experimental results greatly validated the model and confirmed that a plug flow condition existed within the screening zone. This model was further verified in a study of reject thickening and fractionation by Wakelin and Corson [45].

Olson et al. [46] proposed an extended concept, "fibre passage ratio", based on the fundamental studies which showed that fibre passage through small apertures is strongly dependent on fiber length [41,42,48,49]. "Fibre passage ratio", which considers the fibre length distribution as well, is defined as the concentration of fibres of length l, passing through a single aperture, $C_s(l)$, divided by the fibre concentration approaching an aperture, $C_u(l)$."Fibre passage ratio" is more advantageous in quantifying fibre fractionation compared to the bulk passage ratio [47,50,51].

Passage ratio was sensitive to pulp type, screen plate design, feed consistency and other screening parameters [42,46,48,50,51,52]. A theoretical expression for fibre passage ratio was derived based on a fibre length dependent concentration gradient at the screen plate surface [51]. This theory demonstrated that fibre passage ratio is a function of slot geometry, fibre length, slot fluid velocity, and rotor tip speed. Another model based on the "wall effect" and "turning effect" was developed by Olson and Kerekes [50]. This model can predict the fiber passage ratio through a single aperture given the initial position and orientation of a fiber, fiber length, and slot width.

2.2.2.4 Changes in pulp suspension properties

The physical properties of the pulp suspension, such as consistency and pressure difference, undergo changes in pressure screening, both in the axial and radial directions with respect to the screen basket [53].

The consistency in the accept is significantly less than that in the feed, and consequently, the reject consistency increases dramatically [34]. The consistency drop does not change much for reject ratios in the normal operating range (10-30%). However, the relationship between the consistency drop and the accept flow rate is somewhat surprising. It was independent on the accept flow rate for a smooth holed plate, while very sensitive for a contoured slotted plate. Rotor speed has an obvious effect on the pulp consistency change in pressure screens [39]. An increase in rotor speed reduced reject thickening and increased the accept consistency proportionally.

The pressure difference across the screen plate was varied in the axial direction [39]. The highest pressure was recorded in the middle of the screen and the lowest at the end of the screen basket.

2.2.3 Performance of pressure screens

The principal criteria of screen performance are: 1) reject rate, which is the relative amount of good pulp fiber that is rejected with the contaminants, 2) contaminant removal efficiency, which is the percentage of contaminants that leave the screen in the reject stream, and 3) capacity, which is the mass flow rate of pulp in the accept stream.

2.2.3.1 Reject rate

Reject rate is an important and widely used operating variable for industrial screens. It has a clear effect on the accept and reject consistencies. An increase in the reject rate lowered the average pulp consistency in the accept chamber, while the thickening rate towards the reject end of the screen basket increased as the reject rate decreased [39].

Reject rate is related to the operating parameters of pressure screens. For example, Repo and Sundholm [54] reported that with lower rotational speed, it was not possible to achieve as low a reject rate as with the higher rotational speed. This was caused by the smaller pressure pulse from the foil on the rotor. From an operational point of view, reject rate determines the degree of fractionation of the pulp, and the operating range in which screening is possible without plugging [55].

2.2.3.2 Efficiency

The screening efficiency is described by two parameters, cleanliness efficiency, E_c, and contaminant removal efficiency, E_r. The definitions of these two efficiencies are:

$$\begin{aligned} E_c &= 1 - \frac{S_a}{S_i} \\ E_r &= \frac{S_r}{S_i} \times R_W \end{aligned} \tag{2.10}$$

Where S_a, S_i and S_r represent mass fraction of contaminants in the accept, inlet and reject streams, respectively. R_W is the mass reject ratio.

Considering the confusion of the two different efficiencies in common use, and their characteristic that both of them are tied to the reject rate, Nelson [56] developed a single number index, the screening quotient Q. The screening quotient is defined as the ratio of the cleanliness efficiency to the contaminant removal efficiency.

$$Q = \frac{E_c}{E_r} \tag{2.11}$$

The quantity of Q can evaluate the effectiveness of screening. The condition $Q = 0$ describes a screen without a screen plate in it. The condition $Q = 1$ is the theoretical condition for a perfect screen. It rejects every piece of debris without losing a single good fiber. Generally, the value of Q is around 0.9 for an average performance of an average screen on a typical screening application.

With the advantage of being independent of reject rate, the screening quotient has been widely used for modeling screening systems [57,58,59]. Though the screening quotient was created to describe the efficiency of contaminant removal effect of the pressure screens, it is also useful to describe the performance of fractionation [60].

The screening efficiency is dependent on not only the screen design and rotor configuration, but also furnish properties and operating conditions. The aperture dimension and velocity have marked influence on the screening efficiency [42,48,60]. Kumar et al. [35] proposed that for smooth-surface holed baskets, the aperture size should be less than half of the target fiber length, and aperture velocity should be less than 30% of tangential velocity just above the screen plate in order to achieve efficient separation. Sloane [60] found that long fiber fractionation efficiency increased with decreasing aperture size for smooth-surface basket. He also concluded that the rotor shape had a great effect on the screening efficiency, while the rotor speed did not. However, other research work [54,61] reported that lower rotational speed would increase the separation efficiency by controlling the intensity of mixing at the screen-plate surface. Similarly, the passing velocity through the screen plate has a contradictory result on the contaminant removal efficiency. According to Levis [62], increasing passing velocity has no effect on the screening efficiency for non-deformable contaminants, while decreasing the deformable contaminants removal efficiency. In contrast, Vitori [63] found that passing velocity had little effect on the removal efficiency for deformable contaminants. This phenomenon was studied by Yu et al. [31]. He found that the disagreement of the above conclusions resulted from the passing velocity through apertures. Actually, the aperture velocity itself is a dependent variable. So his conclusion was that the dependence of contaminant removal efficiency on the passing velocity was a function of the operation conditions (furnish type, consistency, rotational speed of rotor) and the hardware (types of screen, type of rotor). This is because that passing velocity, calculated by dividing the accept flow rate by the effective open area of a basket, is a reliable variable dependent on those parameters.

The screen plate profile has a significant effect on screening efficiency. Contoured plates are reported to increase greatly the contaminant removal efficiency of pressure screens while decrease the fractionation efficiency, because the long fibers tend to go through the apertures more easily [25,28]. However, according to Niinimaki et al. [64], greater profile roughness led to a decline in contaminant screening efficiency, which is due to an increase in turbulence in the screen basket along with the increase in surface roughness. So in this case, the right choice of contour design is an important decision since one design is not necessarily always the best for every application.

2.2.3.3 Capacity

The maximum capacity of pressure screen is limited by the blinding phenomena. This refers to the accumulation of fibres and fibre flocs in the slots which are not removed by the backflushing pressure pulse of the rotor. It results in permanent screen plugging or blinding which leads to the failure of the screen. Capacity and efficiency are related. Capacity can be traded for efficiency by decreasing the size of the apertures W.

Total screen capacity is directly related to the size of the screen, i.e., bigger screens have higher capacity. However, many factors influence the maximum capacity per area of screen plate, such as the design of the screen apertures, the rotor speed, the gap between the rotor and the screen plate, the slot velocity, the type and the characteristics of the furnish, the consistency at the reject port, etc.. Most of these parameters have been widely investigated [33,64,65].

The open area of the screen plate has a dominant influence on capacity. Generally speaking, the more the open area is, the greater the capacity [65]. However, the slot spacing (i.e., the center-to-center distance) also plays an important role on the capacity. Gooding and Craig [66] found that screen plate blinding was dependent on the percentage of fibers longer than the slot spacing. Severe blinding will occur when 30% of the fibres are longer than the slot spacing. Accordingly, to obtain increased capacity by increasing the number of slots (i.e., increase the open area) may lead to the opposite. Therefore, the slot spacing should be chosen with regard to the fibre length distribution of the feed pulp.

As indicated in the previous part of this review, screen plate contours and some improved rotor design can increase the pulp screen capacity [25,28,33].

A theoretical model of the pressure screen capacity based on the force balance in a single slot was offered by Martinez et al. [65].

$$Q_{\max} = A \cdot \sqrt{\frac{2}{\rho K_H}} \cdot \sqrt{P_P - 2\mu\sigma \frac{T}{W}} \tag{2.12}$$

where

$Q_{\max}$	=	maximum screening capacity
A	=	screen plate open area
T	=	thickness of the aperture throat
W	=	slot width
ρ	=	density of pulp suspension
μ	=	static coefficient of friction
σ	=	compression stress in floc
K_H	=	hydraulic resistance
P_P	=	suction pulsation pressure

Equation (2.12) explains that the pressure screen capacity is potentially determined by three factors: an area term, a resistance term, and a force term. However, there is no clear relationship between the fibre properties and screen design and these terms.

The studies of relationship between the fibre flexibility and the screen capacity showed conflicting results. An industrial study indicated that lower pulp kappa numbers (i.e., increased fiber flexibility) reduce screen capacity [26]. On the contrast, experiments by Gooding and Kerekes [41] confirmed that more flexible fibers tend to pass through the slots.

2.2.4 Power consumption of rotating devices

The challenge for equipment manufacturers today is to design pressure screens to provide the highest capacity, the required level of efficiency while consuming minimal energy.

According to Yu [31], the overall energy loss across the screen can be measured as the inlet pressure less the accept pressure $(P_I - P_A)$. The overall energy loss can be divided into two parts, the energy loss inside the basket and the work input from the rotor. The energy loss inside the screen is due to friction loss (flow through screen openings, flow between rotor and screen basket), dissipation of turbulence, and pressure drag. The relationship can be expressed in Equation (2.13).

$$P_I - P_A = (L - W_R)/(Qt) \tag{2.13}$$

where

P_I = work input from pump (inlet pressure)

P_A = work output (accept pressure)

L = energy loss inside basket

W_R = work input from rotor

Q = flow rate

t = time.

The power consumption of pulp suspension mixing has been studied in several papers. Harkonen [18] measured the shaft torque (shear stress) and the rotating speed (shear rates) in a concentric cylinder shear tester. The pulp suspension was observed to become full turbulent at each consistency when a certain speed was exceeded. This point, characterized by a sharp torque increase, was defined as the "point of fluidization". The power requirement after fluidization, which closes to that of water, can be generalized as:

$$P = \frac{\pi}{15} \cdot V \cdot \tau_D \cdot n_F^{-1.9} \cdot n^{2.9} \tag{2.14}$$

where: V is the volume of the vessel,

τ_D is the disruptive shear stress of pulp suspension,

n_F is the rotational speed at the fluidization point,

n is the practical rotational speed above fluidization point.

Both τ_D and n_F strongly depend on the pulp consistency. Therefore, the power consumption in a mixing vessel depends on the vessel volume, the pulp consistency and the rotational speed.

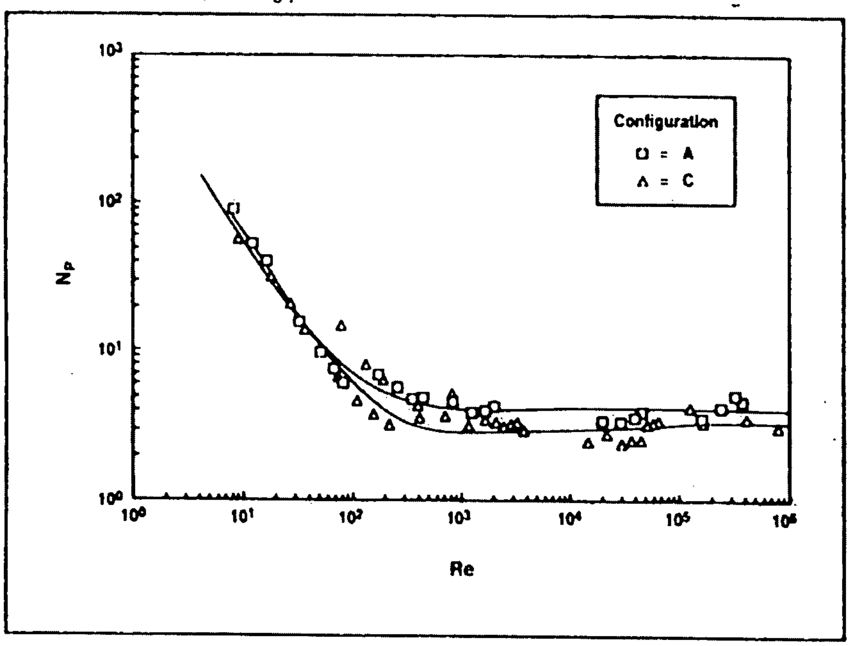

Figure 2.9: Rotor power number versus Reynolds number for the rotor/housing configurations A and C. Fluids used: water, water/Glycerol solutions, Shell Omala 1000, Dow Corning 200 [21].

Furthermore, measuring the power requirements in a similar apparatus, Bennington and Kerekes [21] characterized it by a power number-Reynolds number relationship. The power number, N_P , is given as:

$$N_P = P/(D^5 N^3 \rho) \tag{2.15}$$

The $N_P - R_e$ relationship, presented in Figure 2.9, was obtained using several Newtonian fluids of increasing viscosity (water, water/glycerol solutions, Shell Omala 1000, and Dow Corning 200 Fluid). The power numbers in the fluidized regime of pulp suspensions were found to be identical to those for water in turbulent regime. This confirms that the fluidized pulp suspension did indeed behave as a turbulent viscous fluid.

2.3 Couette-Taylor flow

2.3.1 Introduction

The Couette-Taylor system has played an important role in the development of some of the fundamental concepts of fluid mechanics. Couette-Taylor flow is the flow between concentric rotating cylinders. With its simple geometry and high symmetry, Couette-Taylor system has great advantages in experimental studies. The most commonly employed experimental Couette-Taylor system has a rotating inner cylinder while the outer cylinder is fixed. Therefore, the Reynolds number can be defined as

$$R_e = \frac{\Omega a(b-a)}{\nu} \tag{2.16}$$

where Ω is the rotation rate of the inner cylinder, a and b are the radii of the inner and outer cylinders, and v is the kinematic viscosity of the fluid. The radius ratio of Couette-Taylor system is defined as $\eta = \frac{a}{b}$.

Couette-Taylor flow has been studied extensively at both low and high Reynolds number, and throughout transition. The seminal work of Taylor in 1923 demonstrated that the laminar Couette state undergoes a transition to an axially periodic state, Taylor vortex flow. The next transition will lead to a state with waves on the vortices and that multiple wavy vortex flow states could be stable at a given Reynolds number [71]. Above this state, the higher Reynolds number introduces higher instabilities to the flow and finally reached the transition to turbulent Taylor vortices [72,73,74].

2.3.2 Torque scaling and power law fitting

Since Couette-Taylor flow is a shear-driven flow, torque scaling is of great help to understand its behavior. Traditionally, the torque scaling is defined as:

$$G = \frac{T}{\rho v^2 L} \tag{2.17}$$

where T is the torque, ρ is the fluid density, and L is the axial length of the inner rotor.

Wendt [75] performed torque measurement in the Couette-Taylor system at Reynolds number ranging from 50 up to 10^5. Three different radius ratios were used, $\eta = 0.680,\ 0.850$, and 0.935. He applied non-dimensional torque G in the measurements data fitting with an uncertainty of 3%:

$$G = \begin{cases} 1.45 \dfrac{\eta^{3/2}}{(1-\eta)^{7/4}} R_e^{\,1.5} & for\ 4\times10^2 < R_e < 10^4 \\ 0.23 \dfrac{\eta^{3/2}}{(1-\eta)^{7/4}} R_e^{\,1.7} & for\ 10^4 < R_e < 10^5 \end{cases} \tag{2.18}$$

Measurements by Taylor [76] covered the same range but were not fit to any empirical expression.

Tong et al [77] measured the wall stress T_w on the rotating cylinder in polyethylene oxide dilute solution, and reported power-law scaling of $G \sim R_e^{\,1.8}$ over the range R_e=$3.3\times10^4 \sim 3\times10^5$. Different from traditional definition of Reynolds number in Couette-Taylor flow, the Reynolds number here is defined as $R_e = \omega a^2 / \nu$. As their measurements of wall stress from the motor power, there were several compounding errors: efficiency losses, drag from bearings and seals, and drag from the end sections.

By assuming that the gap between the outer and inner cylinder is divided into three radial regions: two thin boundary layers, one near the inner cylinder of thickness δ_{in} and one near the outer cylinder of thickness δ_{out}, and an inviscid core separating them, Marcus [78] calculated the Couette-Taylor system and predicted that $G \sim R_e^{\,5/3}$. A similar scaling result was obtained by Barcilon and Brindley [79].

All the measurements showed that the torque scaling fits power-law with Reynolds number $G \sim R_e^{\,\alpha}$, though the exponent remains different. The exponent for $R_e \to 0$ has been known since the work of Couette [80]: $\alpha = 1$. This result is the basis for Couette viscometry. In the opposite limit, the exponent for $R_e \to \infty$ can be derived from

Kolmogorov turbulent theory. Assume that the energy dissipation rate ε is constant within the inertial range, independent of length scale, and given by

$$\varepsilon = \frac{(\Delta U)^3}{l} \tag{2.19}$$

Apply this relation at the largest length scale $l = (b-a)$ and $\Delta U = \omega a$. Equation (2.19) then yields $\varepsilon = (\omega a)^3 / (b-a)$. As the torque is the ratio of total power dissipation over the rotating rate, thus the torque scaling can be expressed as:

$$G = \pi \cdot \frac{\eta(1+\eta)}{(1-\eta)^2} \cdot R_e^{\ 2} \tag{2.20}$$

This calculation is relevant in the limit of infinite Reynolds number, where the viscous effects are negligible, and thus the scaling exponent $\alpha = 2$ might be considered an upper limit. The value of 2 for α was first obtained by Nickerson [81]. Later, Doering and Constantin [82] reported the same result derived directly from Navier-Stokes equation.

Lathrop et al. [83] measured the torque of Couette-Taylor flow in five different fluids over the Reynolds number range $800 < R_e < 1.23 \times 10^6$, shown in Figure 2.10(a). Their measurements revealed that there was no range in R_e for which the toque is described by a fixed exponent, α. Rather, α increased monotonically form 1.23 at $R_e = 2800$ to 1.87 at $R_e = 1.2 \times 10^6$. The exponent can be expressed as following:

$$\alpha = \begin{cases} 1.66 + 0.647 \log_{10} \dfrac{R_e}{R_{eT}}, & for\ R_e < R_{eT} \\[2ex] 1.66 + 0.111 \log_{10} \dfrac{R_e}{R_{eT}}, & for\ R_e > R_{eT} \end{cases} \tag{2.21}$$

The transition at $R_e = 1.3 \times 10^4$ is apparent in Figure 2.10(b) with the local exponent, $\alpha = 5/3$. This value is the same as the calculation by Marcus [78], and Barcilon and Brindley [79]. However, the largest exponent value 1.87 was below the prediction $\alpha = 2$. This indicated that the torque is viscosity dependent which was contrast to the Kolmogorov assumptions, although the dependence was relatively weak.

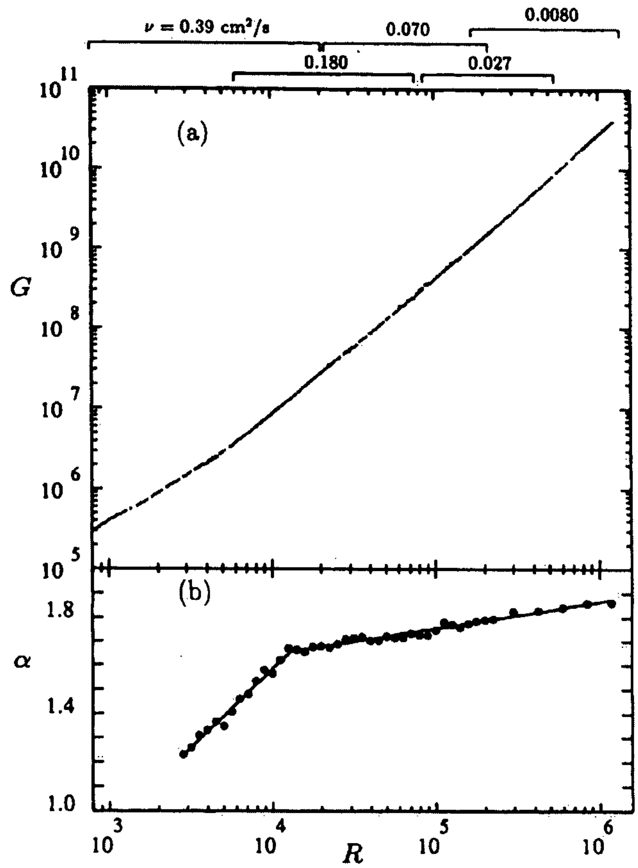

Figure 2.10: (a) the measured non-dimensional toque for the Couette-Taylor flow; (b) the corresponding local scaling exponent α. The straight lines in (b) are given by, for $R_e < R_T$, $\alpha = 1.66 + 0.647\log_{10}(R_e / R_T)$, and for $R_e > R_T$, $\alpha = 1.66 + 0.111\log_{10}(R_e / R_T)$; $R_T = 1.3 \times 10^4$. The horizon bars above the graph indicated the Reynolds number range for each fluid studied [83].

Lathrop et al. [84] have also shown that a prediction for the scaling behavior of the torque above R_{eT} can be obtained by assuming logarithmic boundary layers at each cylinder wall. By treating the core region as an extension of the boundary layers, he arrived at the following relation between torque and Reynolds number:

$$\frac{R_e}{\sqrt{G}} = N \log_{10} \sqrt{G} + M \tag{2.22}$$

where N and M are different functions of the von Karman constant and the geometry, which was obtained from data fitting: $N = 1.56$, and $M = -1.83$. More recently, Lewis and Swinney [85], by solving the equation (2.22), reached a relation for the Reynolds number dependence of the scaling exponent α,

$$\alpha = \frac{2}{1 + \dfrac{2\log_{10} e}{\log_{10} G + \dfrac{2M}{N}}} \tag{2.23}$$

This prediction was proved to agree with the torque measurement better than that of equation (2.21).

2.4 Summary of literature Review

- Pulp suspensions, as a type of Non-Newtonian fluid, have some specific properties. In pipe flow, there exist three flow regions: plug flow, mixed flow and turbulent flow. Its yield stress is dependent on its consistency. When fluidized, the pulp suspension can be assigned a "apparent viscosity". The fiber suspensions show lower friction loss than water in pipe flow, which is referred as "drag reduction".

- A typical pressure screen consists of a screen cylinder and a rotor. The screen cylinder is made of screen plates with holes or slots. There are some special features like elements, hydrofoils or bumps on the periphery of the rotors to create negative pressure pulses. The magnitude of the pressure pulses depends on the rotor shape, rotational speed and the clearance between the rotor and the screen.
- The flow pattern in a pressure screen is controlled by two mechanisms: a "wall effect" that lower the concentration of stiff shive-like fibers in the entering area, and a "turning effect' that cause the fibers to rotate instead of bending as they turn into the slot.
- The performance of a pressure screen is affected by many factors. The "fiber passage ratio" is sensitive to pulp type, screen plate design, feed consistency etc. The "reject rate" is mainly related to the operating parameters of pressure screens. The "efficiency" and "capacity", on the other hand, is dependent on not only the screen design and rotor configuration, but also pulp suspension properties and operating conditions. "Capacity" and "Efficiency" are related, and "Capacity" can be traded for "Efficiency" by decreasing the aperture sizes.
- When there are no any elements or bumps on the periphery of the rotor, the flow in a pressure screen is similar to a typical Couette-Taylor flow in two concentric cylinders. Traditionally, the torque exerted on the inner rotor shaft is scaled by Equation (2.17), and is plotted with Reynolds number based on the tip velocity and spacing between the inner and outer cylinder. The non-dimensional torque has a power-law relationship with Reynolds Number. The exponent, a number between 1 and 2, increases monotonically with the Reynolds number.

2.5 Objective of this research

- To experimentally investigate the factors that influence the torque exerted on the rotor shaft in pressure screens. Two different situations are considered, smooth rotors and rotors with varying height elements on the periphery of the rotor.
- To reveal the correlation between torque and those affecting factors by dimensional analysis. For smooth rotors, non-dimensional torque is considered, while for rotors with elements, the torque coefficient is applied to learn the extra torque caused by the elements on the rotor.

Chapter 3 Experimental Plan

3.1 Introduction

Due to the complexity of the turbulent flow state in pressure screens, together with the special properties of pulp suspensions and the complex geometry, it is impossible to accurately describe the flow phenomenon by theoretical equations and numerical methods. Therefore we have undertaken an experimental study of pulp screen power consumption using a laboratory pressure screen. The results of the experimental study are then presented in the form of a dimensional analysis.

The objective of this study is to experimentally investigate the factors that affect the power consumption of pressure screens. Those factors include pressure screen geometry, such as the rotor diameter, the clearance between the rotor and screen plate, and the element heights, and also include operating parameters like rotating speed of the rotor and fluid rheology. Though the relationship between power consumption and those parameters revealed in this project were based on small-scale laboratory measurements, it may lead to some extent to industrial optimization and design.

This chapter starts with a description of the experimental equipment and the design of the torque measurement system. The experimental procedure and variable parameters are then introduced. Finally, the dimensional groups for data analysis are described. The experimental results will be discussed in Chapter 4.

3.2 Experimental Apparatus

3.2.1 Equipment system

All the experiments were carried out on a Cross-Sectional Screen (CSS). The CSS (see Figure 3.1) is a laboratory screen modeled after a cross-section of a Hooper PSV 2100 pressure screen. The diameter of the test section is 292mm, and the depth is 50mm. A small screen plate (50×60mm) is situated at the bottom of the CSS. The rotor is an aluminum solid-core rotor with two elements located on opposite sides of the outer surface.

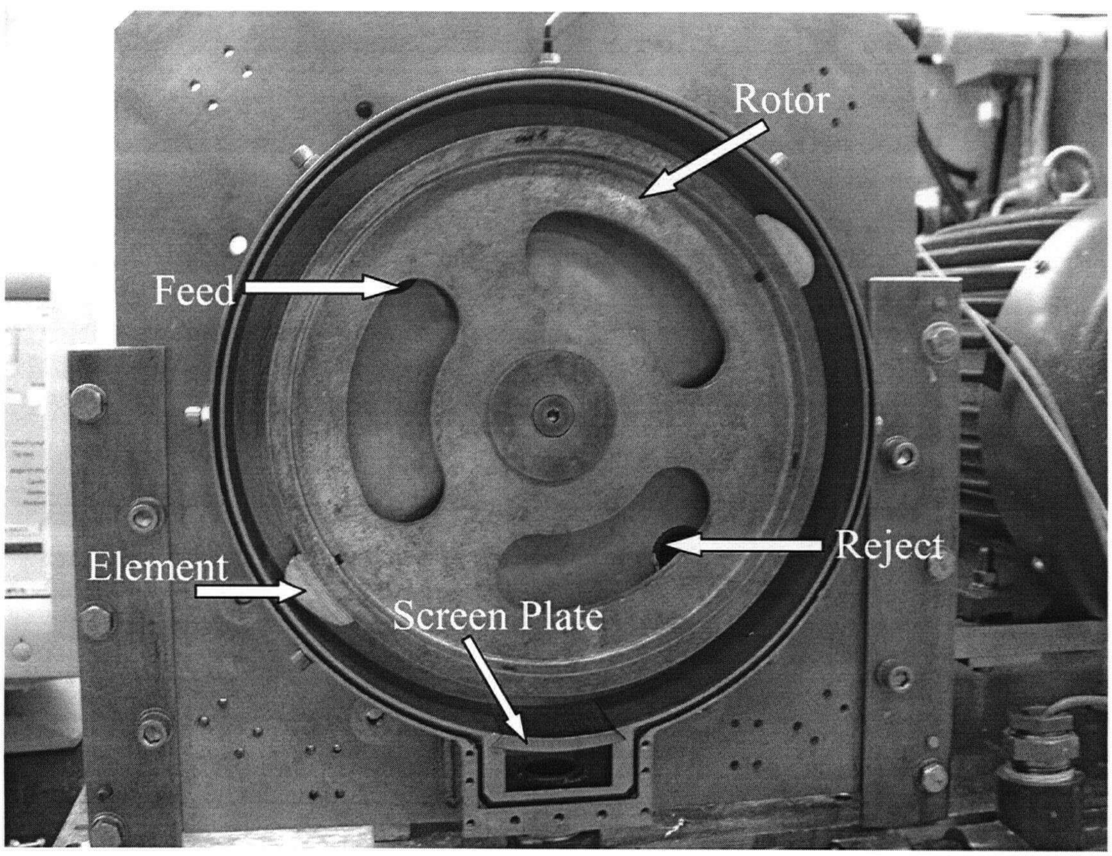

Figure 3.1: Photo of the CSS

Figure 3.2 presents the schematic flow diagram of the CSS. The feed pulp suspension is pumped from the reservoir into the screening cylinder through a 1-inch PVC pipe. There is a control valve on the pipeline to change the feed flow. The feed flow-rate is measured by a magnetic flow meter. The inlet port is located on the upper left quadrant on the back plate of the test cylinder. The reject flow exits the CSS through the outlet port, which is located on the lower right quadrant of the test cylinder, and leads back to the reservoir. The accept flow passes through the small screen plate and also returns to the reservoir. Due to the small area of screen plate, the accept flow in the CSS is much smaller than the reject flow. Both accept and reject flows are controlled by valves. The accept flow rate is measured by another magnetic flow meter (there was no accept flow in these experiments). The reject flow rate is calculated from the difference of the feed and the accept flowrate.

Two pressure transducers are connected to feed and accept pipeline to record the pressure of the feed and accept flow respectively. A high frequency pressure transducer is mounted on the top of the test cylinder.

The outer diameter of the rotor was designed to be adjustable. Aluminum rings of different thickness could easily be added on or removed from the rotor, so that the spacing between the rotor and the outer wall could be changed. Two removable elements were amounted on the outer surface of the rotor symmetrically to simulate industrial pressure screens (see Figure 3.3). By adding shims under the element, the height of the element was also changeable. The rotor was driven by a 10-hp electric motor controlled by a frequency inverter driver. Therefore, the motor speed could be controlled at any speed by changing the frequency.

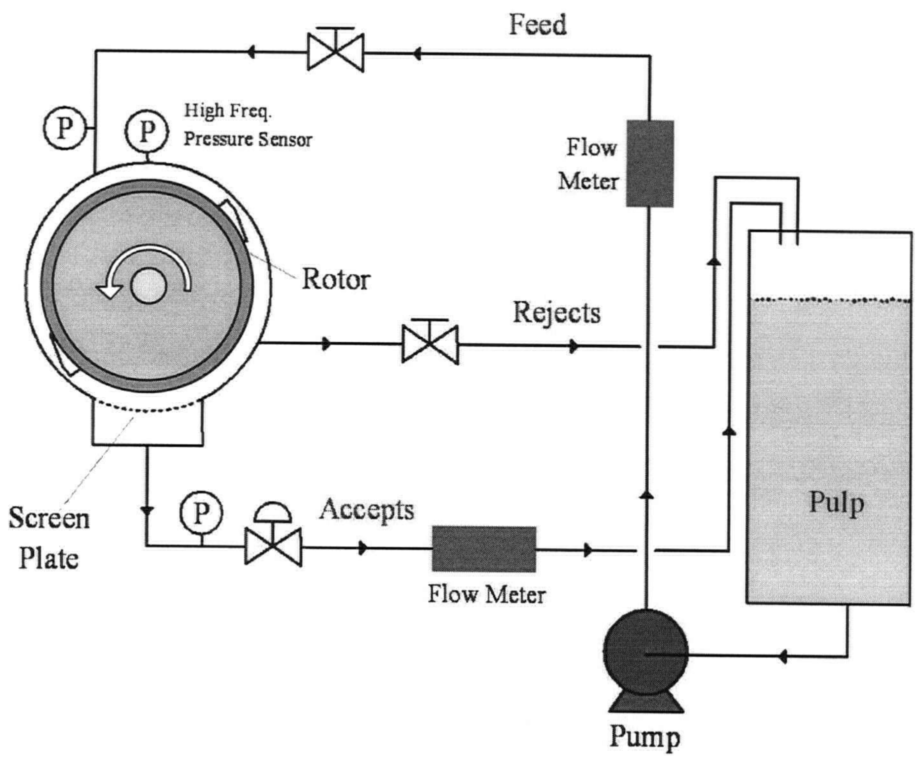

Figure 3.2: Schematic diagram of the CSS (a solid-core rotor with two elements is shown here)

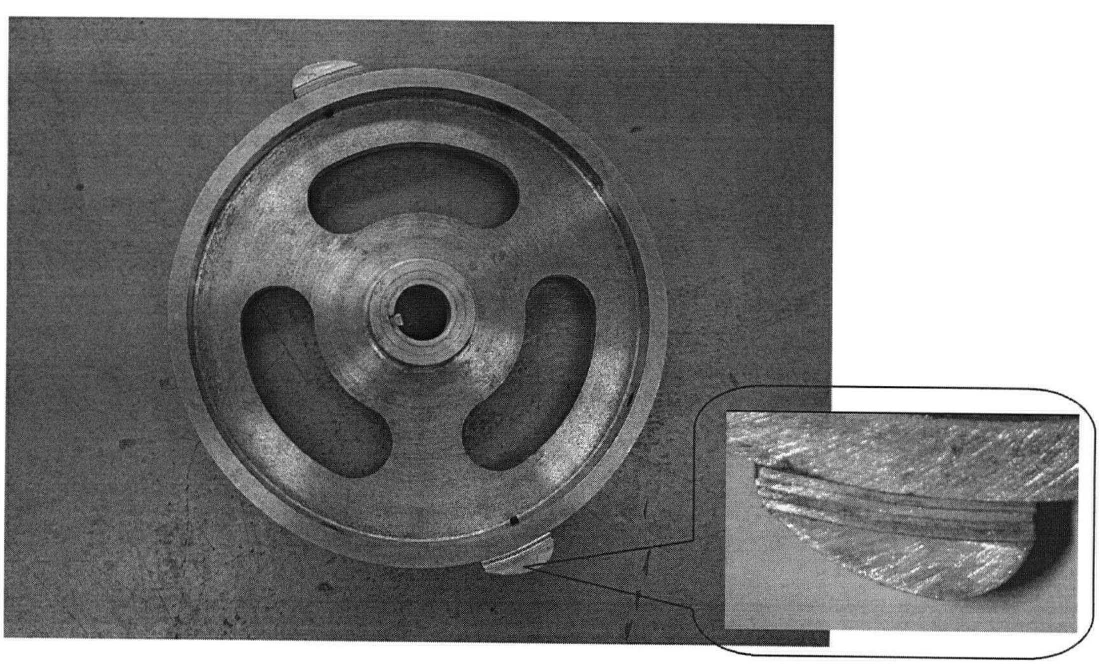

Figure 3.3: The rotor used in this study (showing the two AFT Gladiator shaped elements)

3.2.2 Torque measuring system

A commonly applied means of torque measurement is to measure the strains on the shaft rather than to measure the torque directly. As the torque on a shaft expresses itself by applying forces on it, and forces will cause strains in both parallel and perpendicular direction to the force, the torque therefore is proportional to the strains on the shaft. The strain, which is the amount of deformation of a body, is defined as the fractional change in length. Stain is a dimensionless quantity. The principle strain, $\varepsilon = \Delta L / L$ (L is the body length in the direction of applied force, ΔL is the extended part of length), is the strain in the direction of the applied force, and the transverse strain, $\varepsilon_{\tau} = \Delta W / W$ (W is the body length in the perpendicular direction of applied force, ΔW is the extended length of the same direction), is the strain perpendicular to the applied force. The ratio of the two strains is called Poisson's ratio which depends on the material. Poisson's ratio is 0.285 for steel and 0.32 for aluminum. In practice, the magnitude of measured strain is very small. Therefore, it is usually expressed in microstrain (μe). The value 10,000 microstrain represents a deformation of 1%. can be measured indirectly by measuring the strain on the target shaft, which has been proved to be an effective and accurate means of torque measurement.

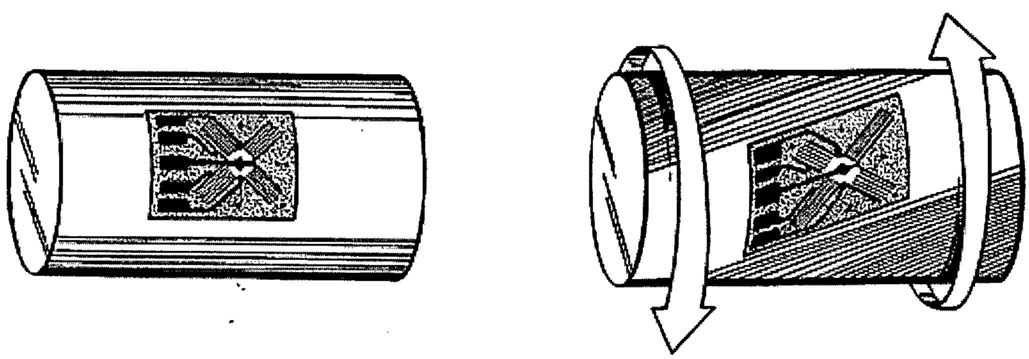

Figure 3.4: Gauge distortion exaggerated [86]

While there are several methods of measuring strain, the most commonly applied way is using strain gauges. A strain gauge is a device where the electrical resistance varies in proportion to the amount of strain in the device. By attaching the strain gauge to the test specimen, the strain experienced by the test specimen is transferred directly to the strain gauge (as Figure 3.4), which responds with a linear change in electrical resistance. However, in practice, the resistance changes are very small; therefore strain gauges are typically used in Wheatstone bridge configurations. By providing an excitation voltage to the bridge, we can generate a voltage across the bridge and thus determine the resistance of the strain gauge.

A fundamental parameter of the strain gauge is its sensitivity to strain, which is expressed quantitatively as the gauge factor (GF). Gauge factor is defined as the ratio of fractional change in electrical resistance to the fractional change in length (strain):

$$GF = \frac{\Delta R / R}{\Delta L / L} \tag{3.1}$$

The Gauge Factor for metallic strain gauges is typically around 2.

In our experiments, we applied a commercial telemetry torque measuring system Torque Trak 9000 from Binsfeld Company for torque measurements. This system is ideal to transmit live torque data from a rotating shaft with high accuracy. The whole system includes a full bridge strain gauge, a transmitter, an excitation battery, and a signal receiver (see in Figure 3.5). The strain on the shaft is transferred to the strain gauge that is carefully glued on the surface of the shaft. The full-scale output voltage is 10.0 V. By featuring digital data transmission, this system delivers a clean, noise-free data signal. Proper installation of the strain gauge and selection of "sensitivity" can give the system measurement accuracy better than $\pm 0.1\%$. The sensitivity of the entire system can be expressed in terms of Torque-Input per Voltage-Output. The sensitivity is determined by two factors: the strain on the surface of shaft caused by the torque, and the amplification level of the strain gauge output. The strain on the shaft is related to the shaft characteristics. We will give details in the following section. For amplification level, the Torque Trak 9000 system provides a field adjustable connection; therefore, the sensitivity can be adjusted with regards of the torque output.

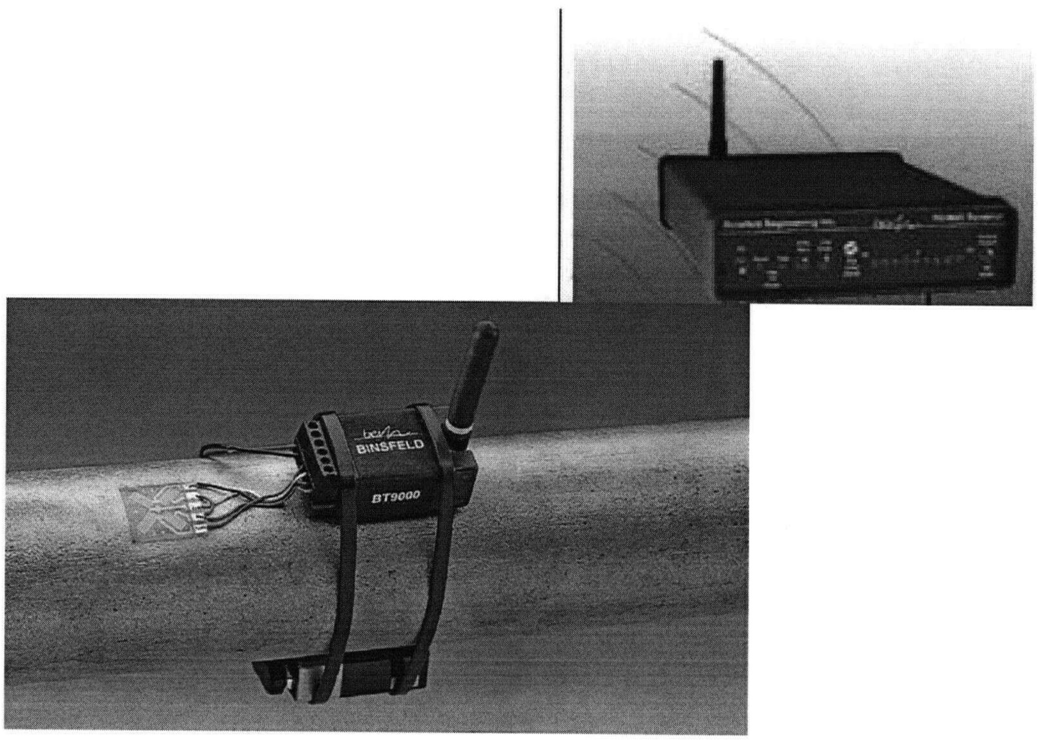

Figure 3.5: The torque sensor (strain gauge) and the transmitter [86]

Stable calibration was taken to test the sensitivity and accuracy of this torque measuring system. Varying standard weights were suspended on the periphery of the rotor by a wire. Therefore, the torque on the rotor can be calculated from the following equation:

$$T = m \cdot g \cdot r \tag{3.2}$$

where, m is the standard weight, g is the gravity, r is the rotor radius.

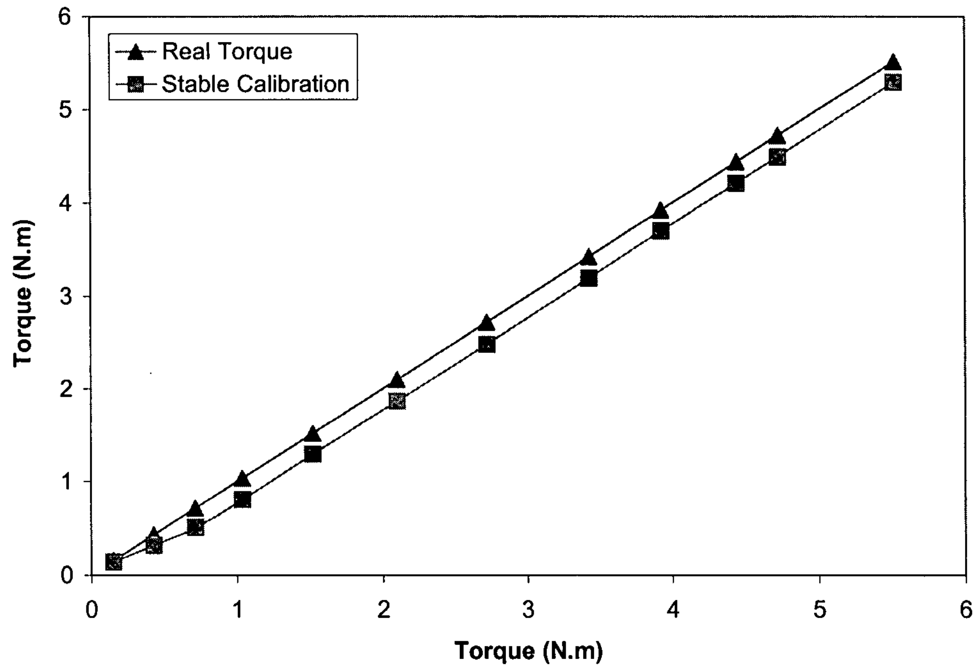

Figure 3.6: Stable calibration for the torque measuring system.

The comparison of calculated torque with the measured torque is shown in Figure 3.6. We find that the measured torque is smaller than the real exerted torque. The measured curve has a smaller slope than that of the real value when the torque range is less than $1\,N.m$, but gets the same slope as that of real value as the torque exceeds $1\,N.m$. In this study, the toque generated by the tested fluid is calculated from the torque difference between the rotor running with the fluid and without the fluid; therefore, this type of measuring error can be eliminated from the calculation.

3.2.3 Shaft design

The strain on the surface of a shaft is a function of torque exerted and the shaft characteristics [86]:

$$\varepsilon_g = \frac{16000TD_o(1+\psi)}{\pi(D_o^4 - D_i^4)E} \tag{3.3}$$

Where, T is the torque, D_o is the outer diameter of the shaft, D_i is the inner diameter of the shaft, ψ is the Poisson's ratio, E is the modulus of elasticity, 206800 N/mm^2.

Table 3.1: Compare the micro-strain at a certain torque value and torque output at the full scale voltage output for different shaft diameters

Shaft Diameter	Micro-strain at load 8N.m	Gain	Torque output at full scale output
1" (25.4mm)	15.62	2000	247.26
		4000	123.63
0.75" (19.03mm)	37.04	2000	104.31
		4000	52.15
0.5" (12.7mm)	125.03	2000	30.9
		4000	15.4

According to Equation 3.3, for a solid steel shaft, the strain is inversely proportional to the third order of shaft diameter. Table 3.1 compares the stain experienced on a steel shaft surface with three different diameters under the same torque, and the torque output at full scale of voltage output (DC 10 V). The Gauge Factor of the strain gauge used in our experiment is 2.07.

From Table 3.1, it is obvious that smaller shaft diameter implies higher sensitivity but less torque measurement range. On the other hand, as the shaft for the existing CSS is 1" (25mm), the only way to get sufficient sensitivity is to reduce the diameter of a part of the shaft and mount the strain gauge in this area. However, this will result in significantly reduced shaft strength. In this case, the shaft diameter should be selected carefully to satisfy the torque measurement range and shaft strength, while provide as high as sensitivity. The approximate maximum motor power output can give an estimation of maximum torque output of $34 N \cdot m$. Therefore, considering all these conditions, we designed a special small diameter area on the shaft for the strain gauge (Figure 3.7). This area has a diameter of $0.75''$ (19.05mm). The reduced diameter shaft is large enough to provide the required strength for the rotating equipment and small enough to provide sufficient sensitivity and accuracy for torque measurement, as well. The strain gauge mounted on the smaller diameter area of the shaft represents a torque output of 5.215 $N \cdot m / V$.

The shaft is supported by two self-aligned bearings. The strain gauge is in the middle of the two bearings close to the right bearing (shown in Figure 3.7). This arrangement is able to minimize the axial toque caused by the weight of the rotor and the support force on the bearings.

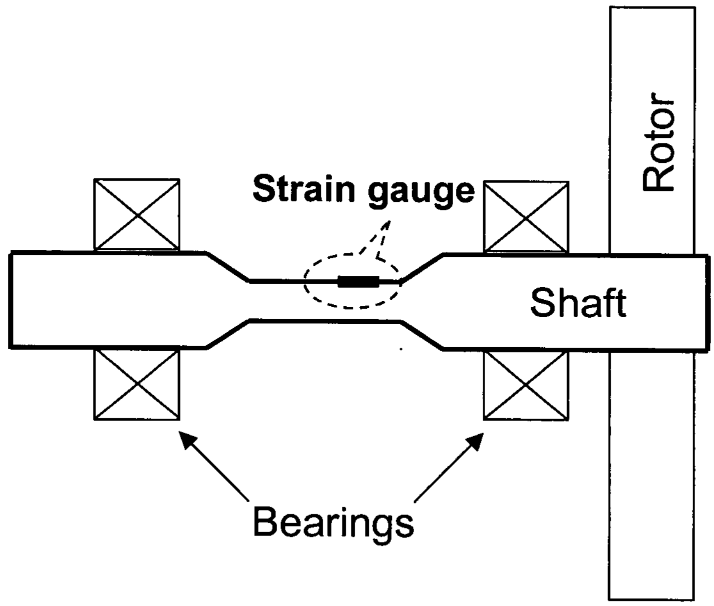

Figure 3.7: Shaft design

3.2.4 Rotating speed control

The rotor in the CSS is driven by a motor that is connected with a frequency inverter driver. Changing the frequency can change the rotating speed of the driving motor. However, the rotor does not always run exactly the same speed as the motor due to the different load from the fluid. There is a small or no deviation at small load while big deviation at high load. Therefore, it is necessary to record the real rotating speed of the rotor. A set of HD25A rugged absolute encoder from US Digital Corp. is installed to record the real revolutions of the shaft during torque measurement. HD25A is a non-contacting optical rotary position sensor which reports the shaft angle within a 360° range. This instrument was first applied in Gonzalez's [43] experiments to measure the pressure pulsations in the CSS.

3.2.5 Data acquisition system

The output voltage signal from the receiver of the Torque Trak 9000 telemetry system, together with signals from magnetic flow meters is connected to a low pass filter module (DBK-18). The module and the optical encoder optical encoder HD25A are connected to a data acquisition card (DaqBoard 2000) installed inside the computer. This data acquisition system is capable of sampling at a rate of 200 kHz. It can support up to 256 analog channels, 40 digital I/O lines and 4 counter inputs, as well as analog, digital or software triggering. The low pass filter module was connected to the analog input channels of the DaqBoard, while the optical encoder was connected to both the digital and counter channels of the card.

3.3 Experiment procedure and plan

3.3.1 Procedure

As the power consumption has a simple relationship with torque:

$$P = T \cdot \omega \tag{3.4}$$

Thus, by knowing the torque and the rotating frequency, it is easy to get the power consumption of the system. Therefore, in the experiment, we focused on torque measurement from which we can calculate power.

A LabView program, which was developed previously (Gonzalez 2002 [43]), was prepared to record all the measured data to text files. This program consists of three main parts: (1) experimental variables include the basic information of the elements; (2) experimental conditions include flow rate, feed and accept pressure, and the rotating speed as well; (3) experimental output includes live voltage and converted torque. The torque module had to be added for these experiments. One hundred torque readings were recorded at each experimental condition in an interval of 1 second. Each data is an average calculated from the collected live torque per 10 ms.

Figure 3.8 shows the interface of the LabView program.

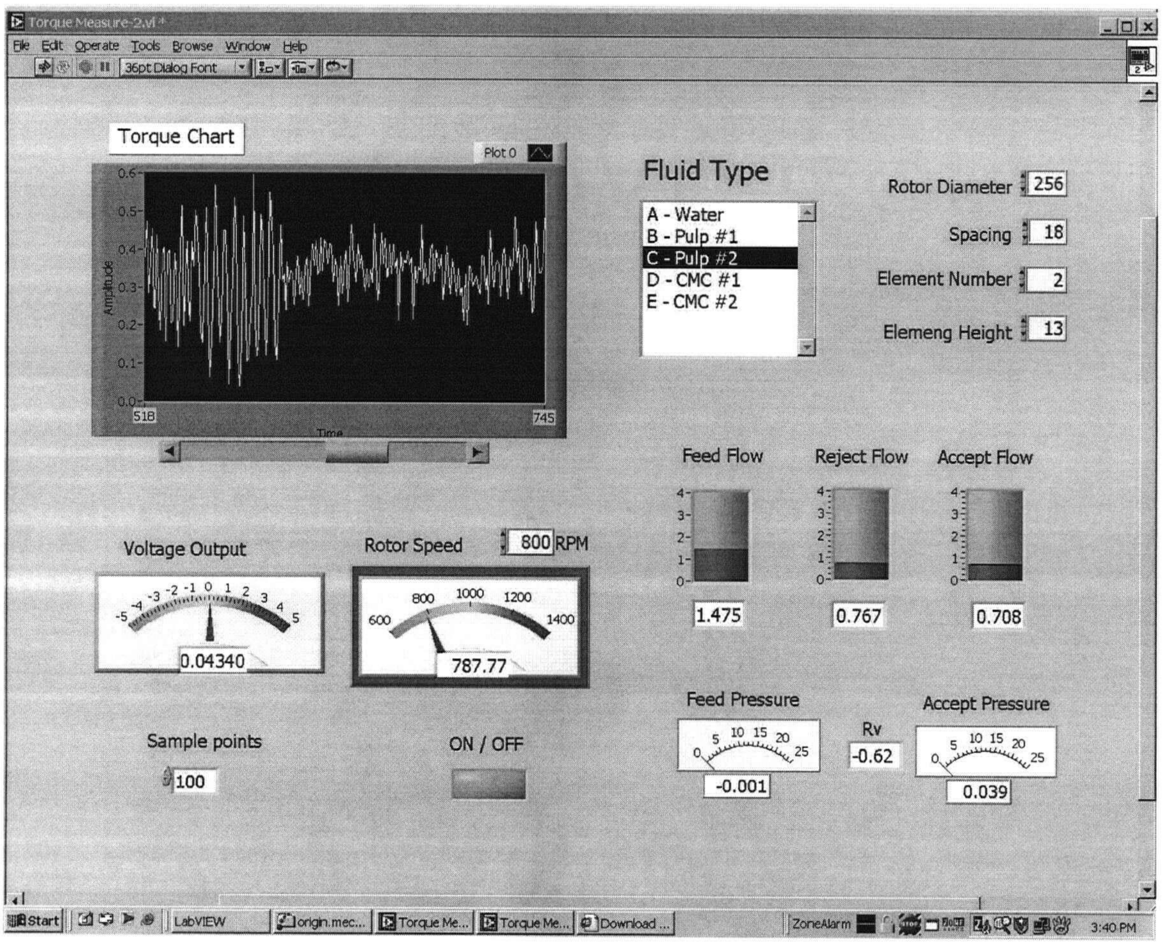

Figure 3.8: Interface of LabView program for experimental data collection

For each rotor design variable and fluid type, torque was measured for a large range of rotating speeds, starting from lower speed to higher speed. For water and CMC solutions, the lower speed is around 50rpm, while for pulp suspensions, the measurable lowest speed depends on the pulp consistency and spacing size for smooth rotor and element height as well for rotors with elements. The higher speed is around 1400rpm for water and CMC solutions running under larger spacing sizes, but lower under smaller sizes, and even lower for pulp suspensions.

As mentioned above, the torque exerted on the running rotor by a specific fluid is calculated form the difference between two measurements: the torque on the rotor running in this fluid, and the torque running at exactly the same conditions in the air. In this way, the errors caused by the weight of the rotor, the friction loss from the bearing and sealing can be excluded from the final torque measurement.

3.3.2 Experimental parameters

The experiments were intended to investigate the factors which affect the power consumption of pressure screens. Therefore, several design and operating parameters will be varied and the resulting torque measured.

The experimental plan can be categorized into two groups: experiments without elements (smooth rotors), and experiments with elements. In each group, the torque measurements were carried out for a combination of different fluids and geometries. In a single measurement, the rotating frequency was set to start with as low as 50 rpm up to 1400rpm. No accept flow was allowed in the loop during experiments, since it does not affect the torque value. Therefore, the reject flow rate is equal to the inlet flow rate. Furthermore, tests showed that the torque on the rotating shaft at full flow rate is the same as that at no flow at all (the CSS basket is full of fluid while both the inlet and reject valves are closed). So, in order to keep the fluid temperature constant or have as slight rise as possible during one measurement, the inlet valve remained fully open. This means that the acceleration of the fluid does not has a significant impact on torque measured and that most of fluid goes straight from the feed to reject port.

3.3.2.1 Fluids

In total five different fluids were studied: water, 1% & 2% bleached softwood Kraft pulp suspensions, 0.2% & 0.5% Carboxymethyl Cellulose (CMC) solutions.

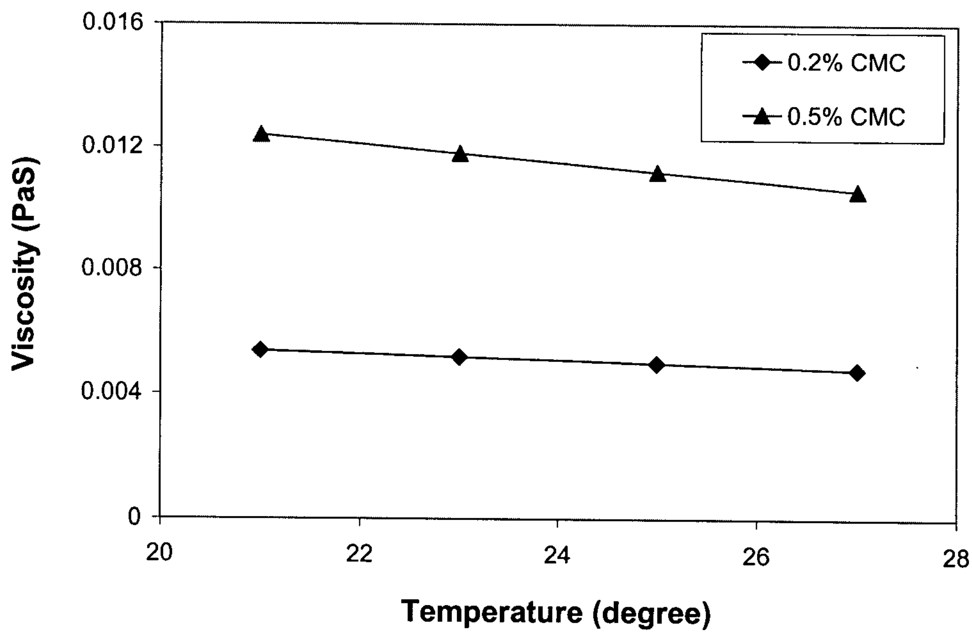

Figure 3.9: The CMC viscosity under different temperatures

The viscosity of the two different CMC solutions was measured by HAAKE Rotary Viscometer. This instrument enables accurate temperature control and gives absolute viscosity data at defined shear rates. There is no temperature control system for the working fluids in our experiment, thus the starting temperature is same as the environment temperature, which is about 23 ℃. However, regarding the slightly temperature rise during single measurement (generally 2 ℃ during running the test from 50rpm to 1400rpm), we tested the viscosity at the temperature range from 21 ~ 27 ℃ (shown in Figure 3.9).

On the other hand, CMC is a shear thinning fluid, which means that the higher the shear rate is, the lower the viscosity. This phenomenon was also detected during the viscosity measurements (shown in Figure 3.10). Since this effect is not very strong, we still use liner regression in determine the fluid viscosity and use the same value in our experimental data analysis.

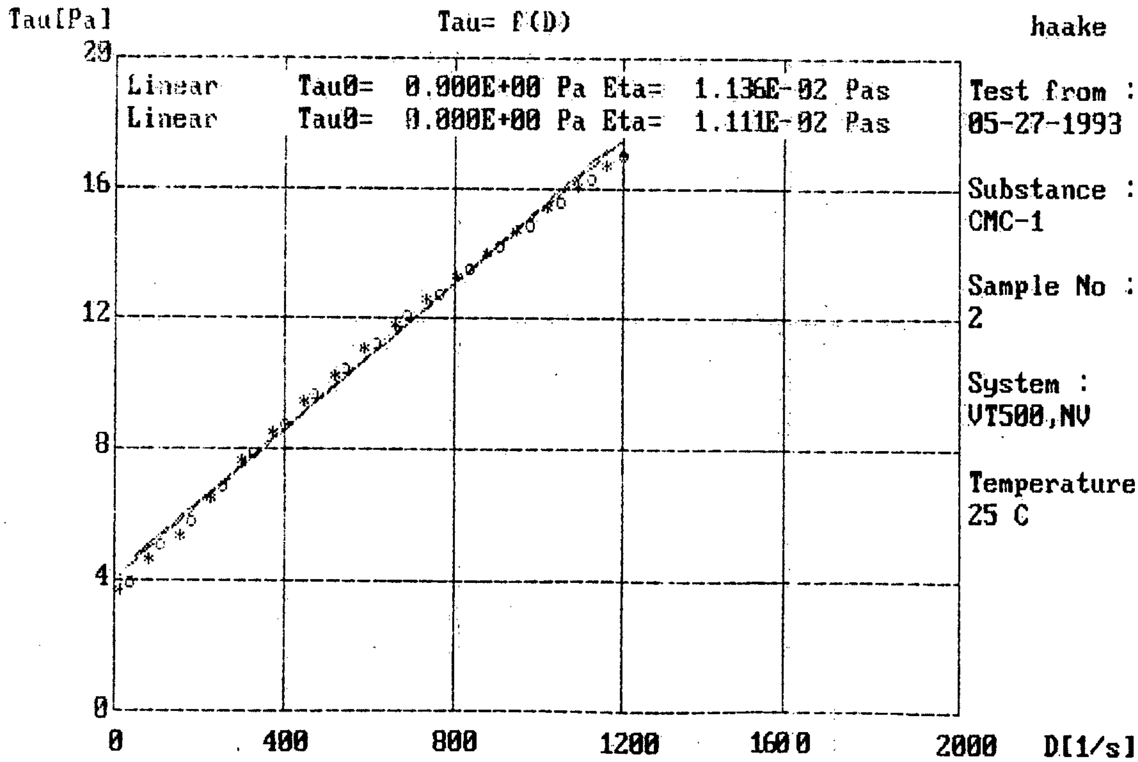

Figure 3.10: Viscosity measurement for CMC by HAAKE rotary viscometer. The sample concentration was 0.5%, and the temperature was 25°C.

3.3.2.2 Geometry

The geometry of pressure screen rotor plays an important role in the resulting power consumption. As mentioned previously, the experiments will investigate both smooth rotors and rotors with elements. For smooth rotors, only the effect of the spacing size between the rotor and the wall of the pressure screen basket will be studied. For rotors with elements, the element height, the spacing between the element and the wall will be studied. The shape of the elements, though also influence the power consumption to some extend, is not considered in this project.

Figure 3.11 shows the geometry of the rotors with elements.

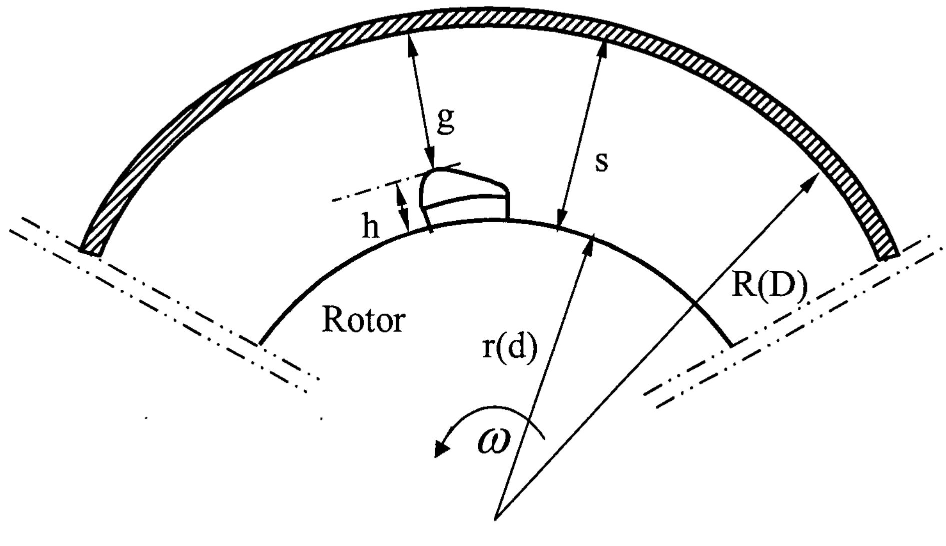

Figure 3.11: Geometry of the rotor with elements

The following table lists all the data of geometry variables for torque measurement in the five different fluids. Due to the plug, some of the measurements for 2% pulp suspensions are not available.

Table 3.2: Geometry parameters for torque measurement in different fluids

	Element Height (h)	Spacing (s)				
		3.6mm	6.8mm	10mm	13mm	18mm
No elements (smooth rotor)	N/A	Yes	Yes	Yes	Yes	Yes
With element	8mm			Yes	Yes	Yes
	10.5mm				Yes	Yes
	13mm					Yes
	15.2mm					Yes

3.4 Data analysis

In order to reveal the correlation between the design and operating variables with power and torque, dimensional analysis was applied to the experimental data. As the different mechanism of smooth rotor and rotor with elements, different dimensionless groups are applied in data analysis.

3.4.1 Smooth rotor

When there is no element on the periphery of the rotor, the flow in the pressure screen basket is very similar to a typical Couette-Taylor flow. Therefore, the torque can be scaled as Equation (2.17B). However, we use T_N as the non-dimensional torque instead of G which was used in the references:

$$T_N = \frac{T}{\rho v^2 L} \tag{3.5}$$

where, T is the toque on the rotor,

ρ is the fluid density,

v is kinematic viscosity of the fluid,

L is the width of the rotor.

For Reynolds Number, there are two options. One option is the equation (2.18), which is based on both the rotor diameter d, and the spacing size $(D-d)/2$. We define this Reynolds Number as R_{e1} in our data analysis:

$$R_{e1} = \frac{\omega d(D-d)}{4v} \tag{3.6}$$

Another one, defined as R_{e2}, is based on only the rotor diameter:

$$R_{e2} = \frac{\omega d^2}{4v} \tag{3.7}$$

Though the parameter $(D-d)$ does not appear in the Reynolds Number #2, it doesn't mean that the varying spacing sizes are neglected. In fact, since the outer diameter is fixed, increasing the diameter of the rotor directly leads to decreasing of the spacing size. As will be shown, Reynolds Number #2 proved more useful than Reynolds Number #1.

3.4.2 Rotors with elements

For rotors with elements, the torque will definitely increase compared to that under the same rotor geometry. This effect results from the drag on the elements. The increasing magnitude of torque depends mainly on the element height, though other factors such as the spacing sizes, fluid viscosity have some influence also. Therefore, a dimensionless torque coefficient (same definition as pressure drag coefficient) will be applied in data analysis for the increasing toque generated by the elements.

$$C_t = \frac{T_e - T_s}{\frac{1}{2}\rho U^2 hld} \tag{3.8}$$

where, T_e is the measured torque of rotors with elements;

T_s is the measured torque for smooth rotor under the same spacing;

ρ is the fluid density;

U is the tip velocity of the rotor which is calculated by $U = \omega \cdot (r + h/2)$

h is the height of the element

l is the width of the element (note that hl is the projected area of the element into the direction of travel of the element).

As that T_N for smooth rotors, the torque coefficient will also be plotted versus the R_{e2} instead of R_{e1}. In general, from our dimensional analysis, we expect that the additional torque from the rotor elements to have the following functional form:

$$C_t = f(\mathrm{Re}, h/D, g/D) \tag{3.9}$$

where, D is the diameter of the screen basket.

Chapter 4 Experimental Results and discussions

4.1 Introduction

The torque on the rotor running in the CSS was obtained for a wide range of design and operating variables, including rotational velocity, rotor diameter (spacing), element height and fluid types. The experimental results are categorized into two groups namely smooth rotors and rotors with elements.

4.2 Smooth rotors

For smooth rotors, the flow in the screen basket is similar to the Couette-Taylor flow. Therefore, the experimental results are going to be analyzed as that for Couette-Taylor flow given in the literature and compared with some experimental results of typical Couette-Taylor flow.

4.2.1 Effect of rotating speed and spacing

The spacing between the rotor and the outer housing is varied by adding rings around the rotor, increasing its diameter. Figure 4.1 shows the measured torque vs. rotating speed for water under five different rotor spacing (rotor diameters). It is clear that decreasing the spacing between the rotor and the outer wall increases the applied torque, though the influence appears to be relatively small. However, this is not in a linear relationship. For lower rotating speeds, the torque decreased approximately to the same level. It is also apparent that for all different spacing, the measured torque approached zero as the rotating speed approached zero.

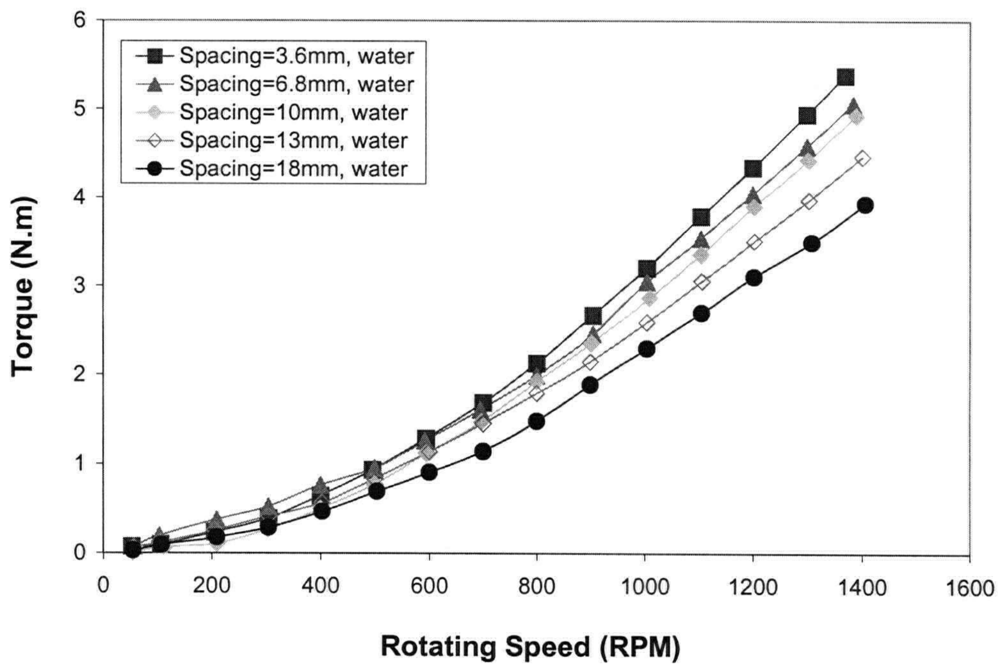

Figure 4.1: Measured torque for smooth rotors of varied gap sizes in water

The torque was scaled using Equation (3.5). For the fluid velocity scaling, two different definitions of Reynolds Number were considered, which were defined in Equation (3.6) and Equation (3.7). R_{e1} is based on the spacing, while R_{e2} is based on the rotor radius. We plotted the non-dimensional torque versus these two Reynolds numbers in Figure 4.2 and Figure 4.3, respectively.

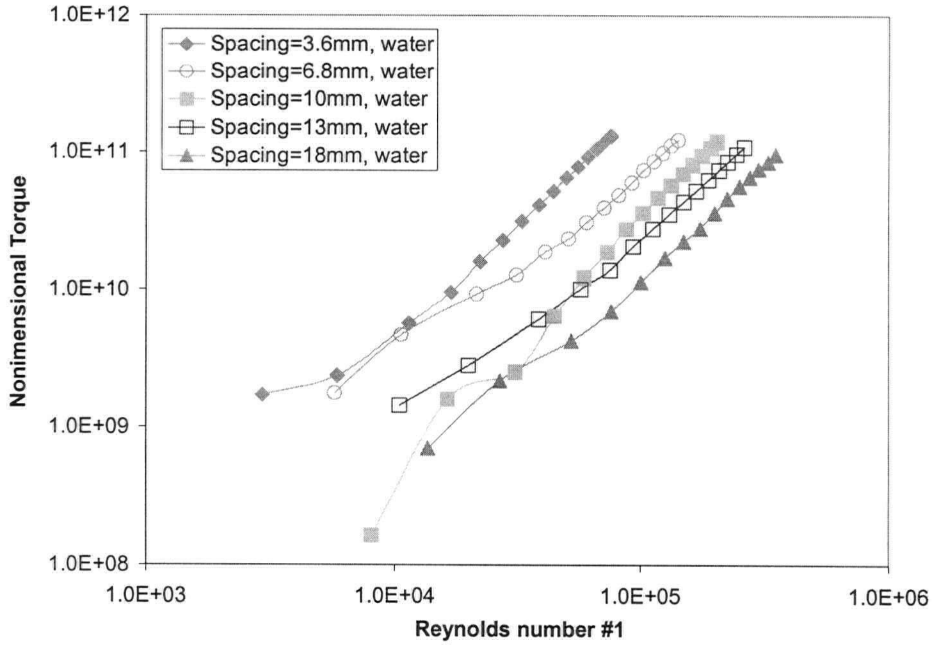

Figure 4.2: Non-dimensional torque vs. Reynolds Number Re_1 for smooth rotors of different rotor spacing in water

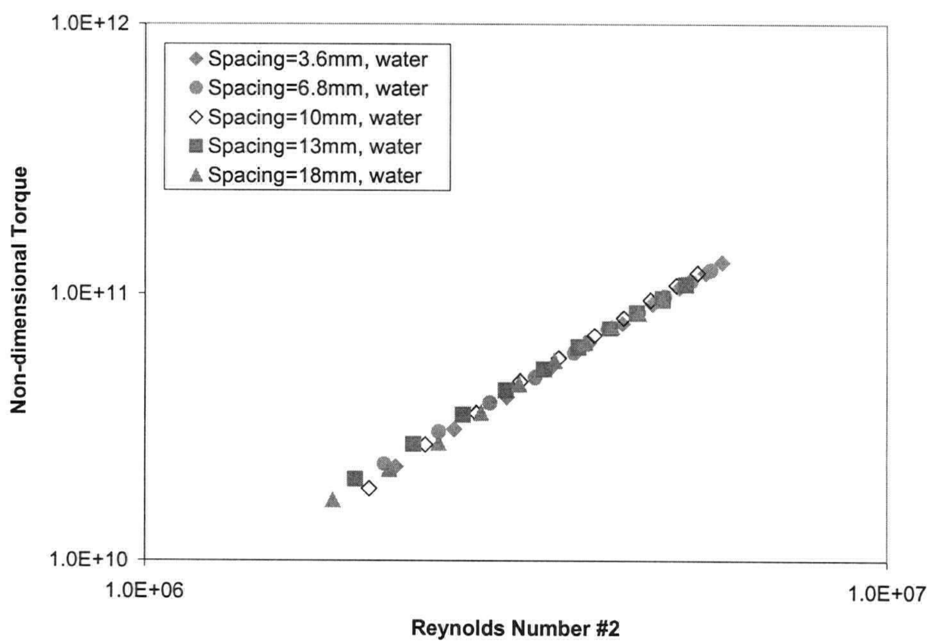

Figure 4.3: Non-dimensional torque vs. Reynolds Number Re_2 for smooth rotors of different rotor spacing in water

From Figure 4.2, we find that the non-dimensional torque is a function of not only Reynolds no.1, but also the spacing scaling:

$$T_N = f(R_{e1}, \frac{s}{R}) \tag{4.1}$$

Where, T_N is the non-dimensional torque, s is the spacing between the rotor and the pressure screen basket wall, R is the radius of the pressure screen basket.

The Non-dimensional torque is also plotted against R_{e2} in Figure 4.3. From this figure we see that the collapses onto a single curve. Therefore, we see that Non-dimensional torque is a function of R_{e2} only, i.e.,

$$T_N = f(R_{e2}) \tag{4.2}$$

Although these two Figures might look contradictory, it can be explained from the definition of Reynolds Number. In our experiment, the diameter of the outer cylinder is fixed; therefore, increasing of the rotor radius resulted in decreasing of the rotor spacing. The correlation between rotor spacing and rotor radius lead to the correlation of R_{e1} and R_{e2} though the radius ratio of the two cylinders η $(\eta = r / R)$:

$$R_{e2} = \frac{\eta}{1-\eta} R_{e1} \tag{4.3}$$

The above relationship indicated that the influence from the spacing was actually included in R_{e2} already. So, Equation (4.2) might be a better way to describe simply the behavior in Couette-Taylor flow.

From Figure 4.2 and Figure 4.3, we know that the non-dimensional torque has a power-law relationship with Reynolds Number: $T_N \sim R_{e1}^{\alpha 1}$, and $T_N \sim R_{e2}^{\alpha 2}$. By applying power-law fitting, we got two same exponent of $\alpha 1$ and $\alpha 2$, which was around 1.68. This result was very close to previous studies in the literature [75-77].

4.2.2 Effect of fluid type

Though the viscosities of both CMC solution and pulp suspension are higher than that of water, the resulting torque measurements were significantly different. Note the viscosity mentioned here for CMC and pulp suspensions are "apparent viscosity" since both of the two fluids are non-Newtonian fluids. Figure 4.4 shows the torque measurements for the smooth rotor operating over a wide range of rotational velocities at a constant spacing of $13\,mm$.

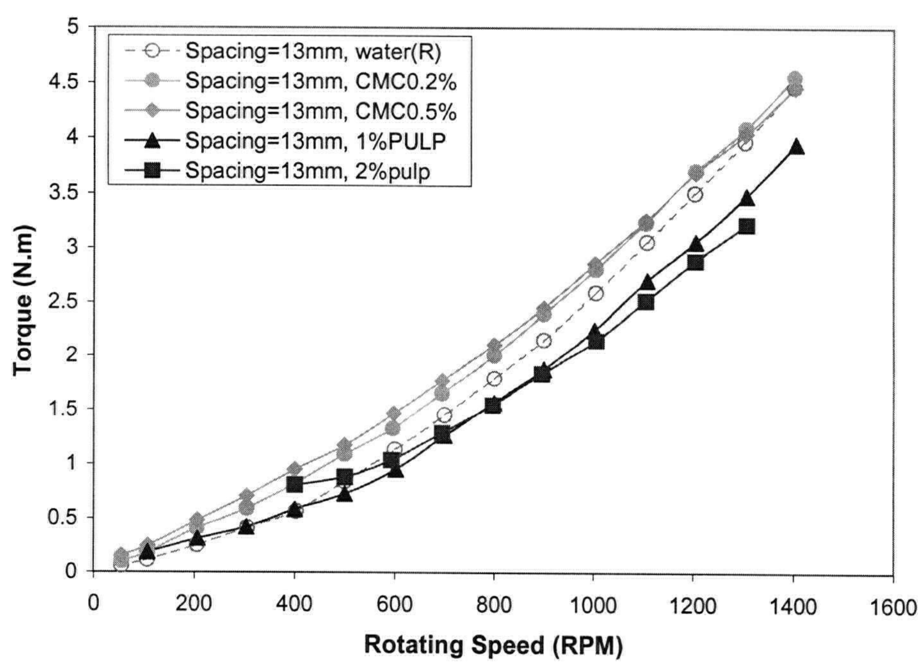

Figure 4.4: The measured torque for smooth rotors running in different fluids. The rotor spacing is 13mm.

From Figure 4.4, we can make the following observations. The CMC solutions, which had higher viscosities than water exerted higher torque on the rotor than water, while pulp suspensions exerted less torque over much of the rotational velocity range. However, both the CMC solutions and pulp suspensions crossed the water line within the experimental rotating range, though at different points: 0.2% CMC solution crossed the water line at about 1200rpm and 0.5% CMC crossed water line at about 1300rpm. These crossing points indicated that the viscosity of CMC solutions was decreasing as rotational velocity increased. This phenomenon is known as shear thinning and is well known for CMC solutions. Pulp suspensions crossed the water line at much lower speed: 1% was around 300 rpm, and 2% was around 500 rpm.

We also observe that the torque-RPM curves for CMC solutions approached zero while the torque line for pulp suspensions did not. The torque does not approach zero for pulp suspensions as they have a yield stress.

For CMC solutions, the higher the viscosity, the higher the observed torque at a constant RPM. This agrees with what is expected from a common understanding of fluids, i.e. high viscosity fluids will require more power than low viscosity fluid under the same operating conditions. However, the same does not hold for pulp suspensions: 2% pulp suspensions exerted less torque than 1% pulp suspension though the viscosity for 2% pulp suspension ($0.0128\, Pa \cdot s$) is about 8 times higher than that of 1% pulp suspension ($0.0015\, Pa \cdot s$), as determined by Bennington [21]. This unusual phenomenon of reduced viscous friction, even for small particle concentrations, is also well known for pulp/fibre suspensions and is referred to as "drag reduction". The same drag reduction occurs in pipe flow and needs to be accounted for when calculating the headloss due to friction in designing piping systems [19, 22].

Figure 4.5 shows the same data plotted in non-dimensional form, using the same non-dimensional torque as before and Reynolds number based on rotor radius, R_{e2}. The spacing was held constant at $13\,mm$. Overall, the non-dimensional torque for all of the fluids nearly collapsed to a single curve. The CMC and pulp suspensions both had a lower Reynolds number than water due to their increased viscosity. The viscosity used to calculate Reynolds Number for pulps was based on the correlation of Bennington [21].

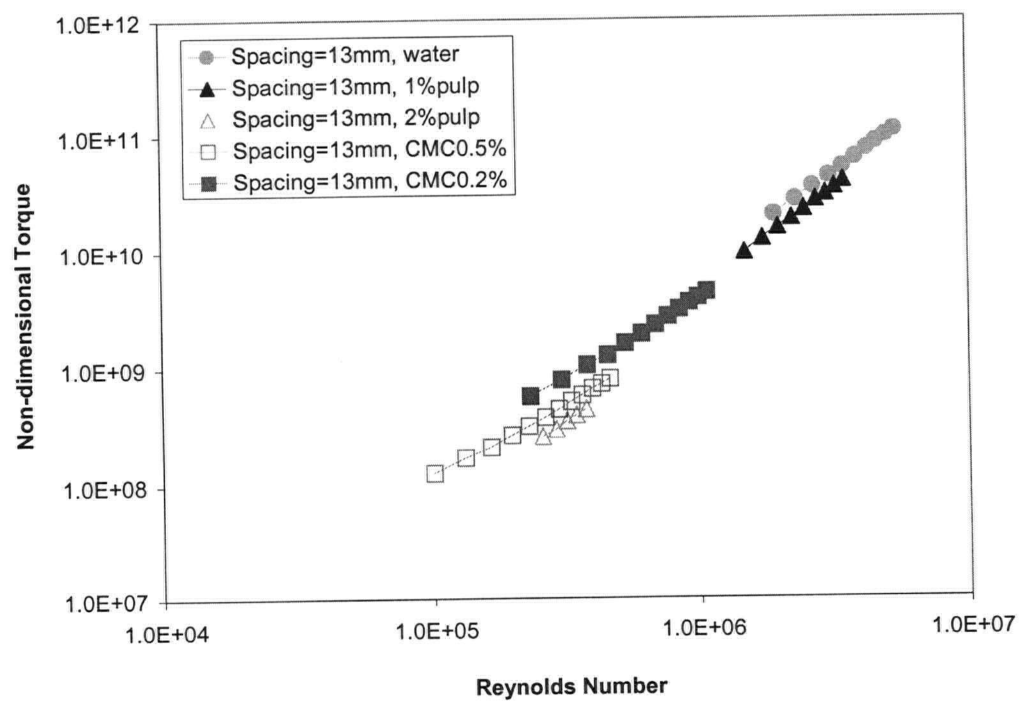

Figure 4.5: Non-dimensional torque vs. Reynolds Number (R_{e2}) for smooth rotors running in different fluids. The rotor spacing is 13mm.

We also note that the non-dimensional torque for all the fluids increase nearly linearly with Reynolds Number on a LOG-LOG plot, thus, the power-law relationship is a good correlation for these data:

$$T_N \sim R_{e2}^{\alpha} \tag{4.4}$$

where, α is the exponent varying with the Reynolds number. A best fit is applied to the data and the exponents are listed in Table 4.1:

Table 4.1: Reynolds Number range and corresponding exponent of tested fluids

Fluid	water	1% pulp suspension	2% pulp suspension	0.2% CMC solution	0.5% CMC solution
R_{e2} 1.00E+05	18 ~ 60	14 ~ 40	2 ~ 4	2 ~ 12	1 ~ 6
Exponent α	1.68	1.62	1.59	1.45	1.32

Figure 4.6 Shows the results of plotting non-dimensional torque against Reynolds number, R_{e2}, for all the fluids and all of the different spacing tested. From this figure we see that, for fluids of different viscosity, the non-dimensional torque can be expressed simply as a function of R_{e2} when the radius ratio is relatively high (the condition for pressure screens). Meanwhile, the relationship between the non-dimensional toque and R_{e2} is a power-law relation with a varying exponent. The exponent increases with the Reynolds Number instead of being a constant. This is similar to the conclusions of previous studies [73,81,82,83] from the relationship between non-dimensional torque and R_{e1}.

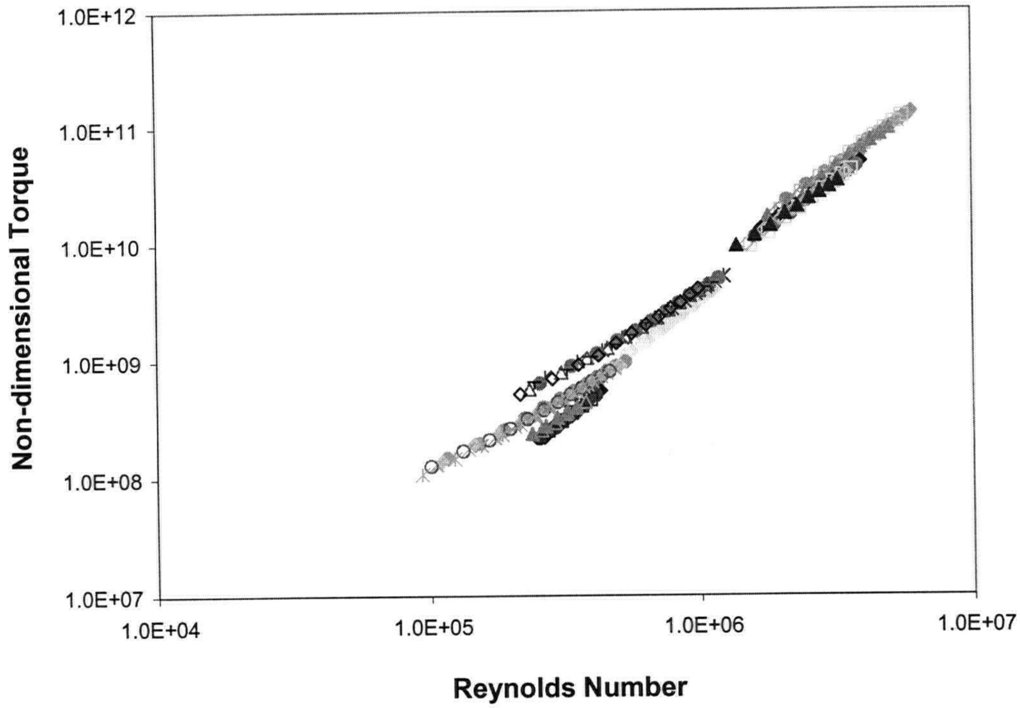

Figure 4.6: Non-dimensional torque vs. Reynolds Number #2 for smooth rotors under different rotor spacing. Totally five fluids tested here: water, 1%pulp suspension, 2% pulp suspension, 0.2% CMC, and 0.5% CMC. The rotor spacing were 3.6mm, 6.8mm, 10mm,13mm, and 18mm.

4.2.3 Summary of smooth rotor results

By measuring the torque on a smooth rotor under different spacing conditions running in different fluids, we discovered that the torque increases quickly with the rotating speed, while the spacing has a relatively slight influence on the required torque. Moreover, the dimensional data analysis revealed the correlation between the exerting torques with the operating conditions. By using the R_{e2} instead of R_{e1}, which was applied in most previous studies, the relationship can be simplified to $T_N = f(R_{e2})$.

4.3 Rotors with elements

Nearly all the industrial pressure screen rotors have protrusions, referred to as hydrodynamic elements, on them that create pressure pulsation and accelerate the fluid at the screen cylinder surface. These elements have an additional drag associated with them; therefore, compared to the smooth rotor, the rotors with elements will require more torque (power) to operate at the same rotational velocity. In this section, we examine the effect of element height, spacing, rotational velocity and fluid type on the additional torque required, and we use dimensional analysis to establish a correlation among the variables.

4.3.1 Effect of element height and spacing

The total torque required to rotate the rotor with varying element heights, at a constant spacing equal to 18 mm, operating in water, is shown in Figure 4.7. There were four different height steps from $8\,mm$ to $15.2\,mm$ in our experiment. Height of $0\,mm$ stands for smooth rotor.

All the torque-RPM curves were originated from almost the zero point, which was in accordance with the feature of Newtonian fluids. However, as the elements on the rotors would generate extra torque on the shaft, the slope of the curves increased with the increasing element height. The higher the elements, the steeper the slope is.

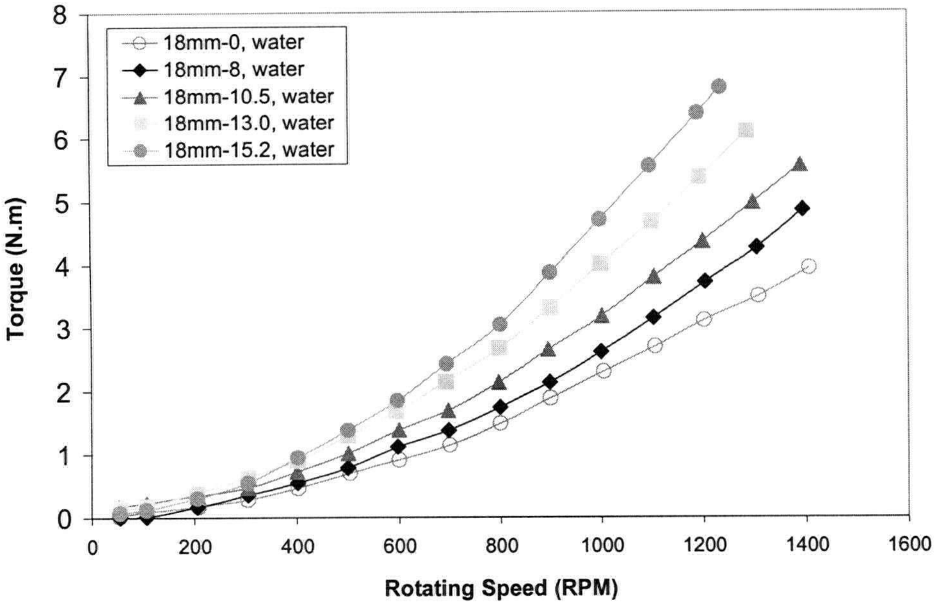

Figure 4.7: Measured torque under constant rotor spacing in water. The rotor spacing is constant at 18mm, and the element heights are 8mm, 10.5mm, 13mm, and 15.2mm. Element height of 0mm represents a smooth rotor.

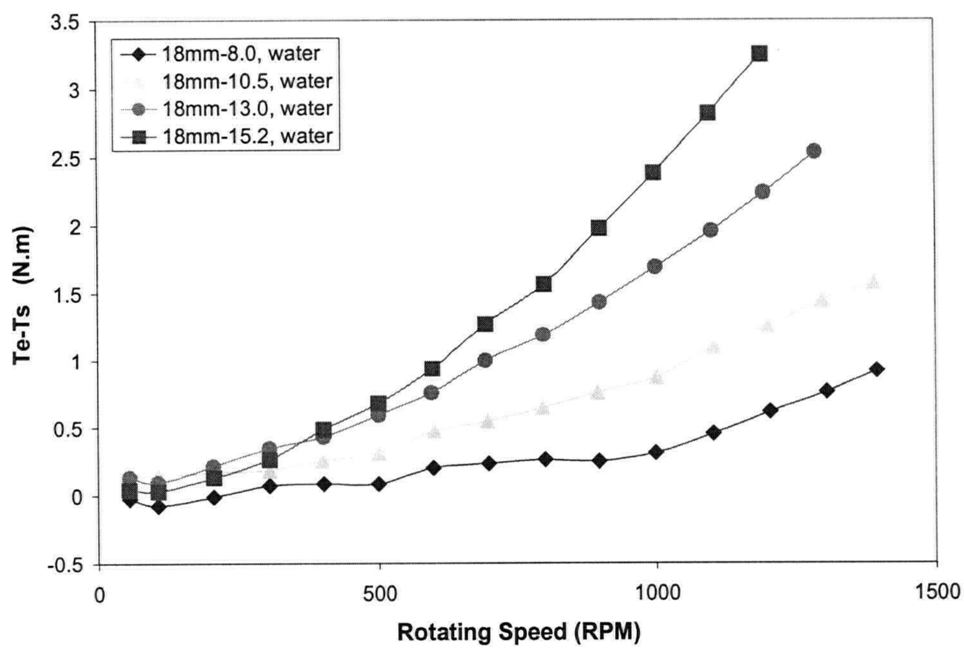

Figure 4.8: The extra amount of torque generated by the elements on rotors running in water. The rotor spacing is 18mm. The element heights are 8mm, 10.5mm, 13mm and 15.2mm.

Figure 4.8 shows the amount of additional torque generated by the elements on the rotor, which is the difference between the torque on a rotor with elements, *Te*, and the torque on a smooth rotor, *Ts*. As expected, we can find that the torque lines become much steeper when the height of the element increases. We assume that the extra torque from the elements was caused mostly by the high normal pressure drag on the leading edge of the element and the relatively low pressure in the region behind the element where vortices are expected to occur.

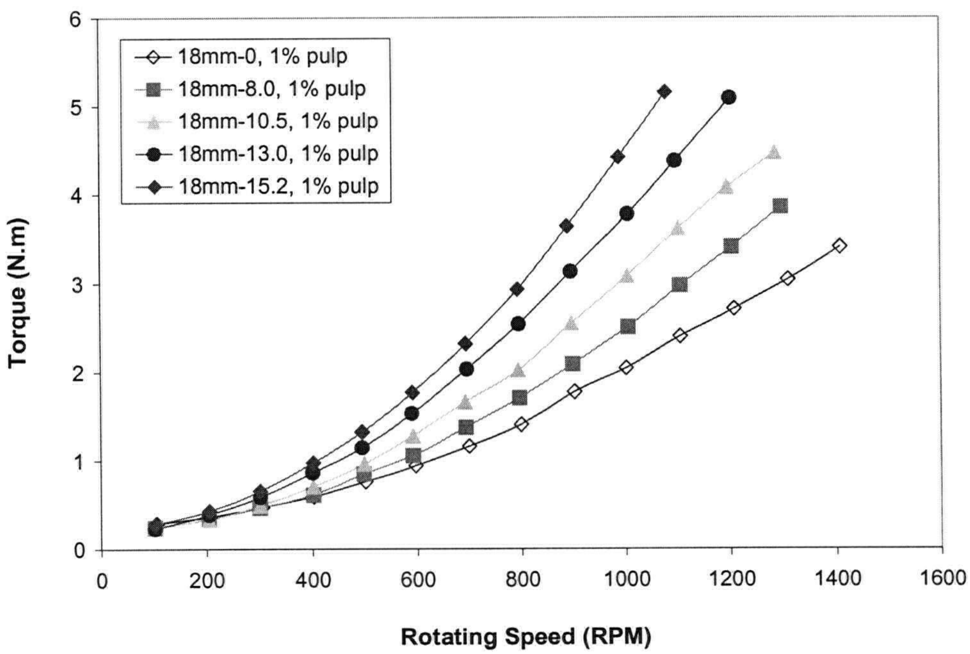

Figure 4.9: Measured torque under constant rotor spacing in 1% pulp suspension. The rotor spacing is 18mm, and the element heights are 8mm, 10.5mm, 13mm, and 15.2mm. Element height of 0mm represents of smooth rotor.

Figure 4.9 shows the torque required for varying element height and constant spacing for 1% pulp suspension. The same observations that apply for water are also shown to hold for pulp suspensions.

The effect of the element height can be further demonstrated by comparing the torque under constant gap (distance between the element and rotor housing). Since the outer cylinder has a fixed diameter, the constant gap is made from different spacing and element heights, which is shown in Figure 3.11. The torque for water under constant gap is shown in Figure 4.10. The experimental results of smooth rotors indicate that the bigger spacing leads to lower torque. However, the opposite was found for rotors with elements. The rotor with a higher element under bigger spacing experiences more torque. We think the higher torque was caused by a higher element, which verifies that the height of element had much greater influence upon the torque rather than the spacing or gap. This trend was also found in other tested fluids.

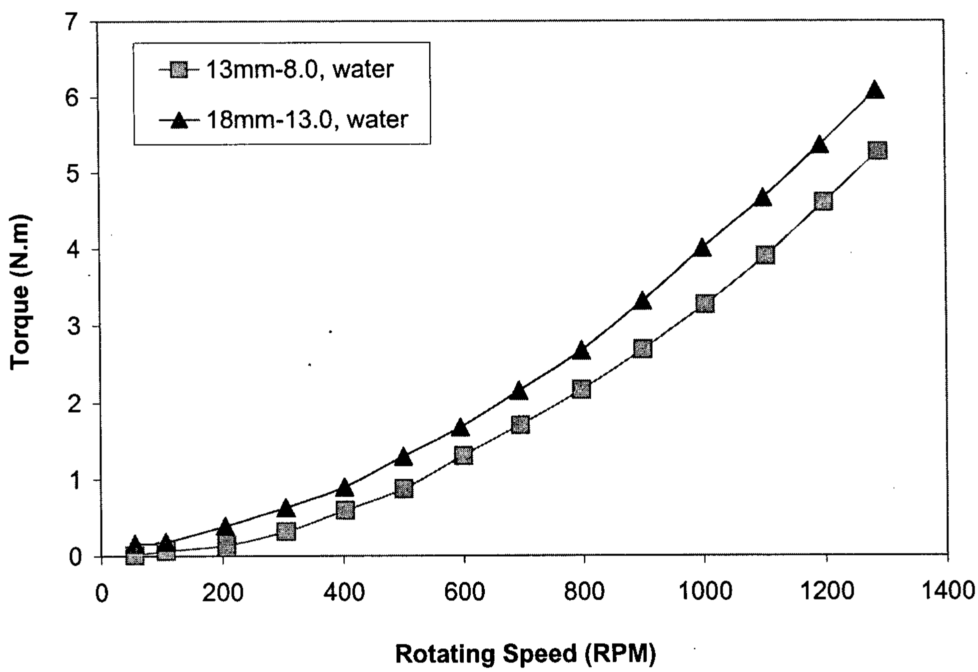

Figure 4.10: Measured torque in water under constant gap made from different combination of rotor spacing and element height.

4.3.2 Dimensional analysis

From the above experimental results, we know that the extra torque for rotors with elements resulting mainly from the normal pressure drag in the leading edge of the elements. Therefore, a dimensionless torque coefficient C_t, which was defined in Equation (3.8) and was based on the normal dimensionless torque coefficient, was employed in this dimensional analysis. The velocity is scaled as R_{e2}, which was based on the rotor diameter.

The relationship between torque coefficient and Reynolds number for water under different geometries was illustrated in Figure 4.11. Except for several diversified dots in the low Reynolds number area of each line, most experiments showed identical trends – they became independent of Reynolds number. In the low R_e range the measured torque was quite small for both the rotor with elements and without elements. Therefore when we estimated the difference between two small measured torques at small Reynolds numbers, the result was a significant increase in measurement noise. This noise sometimes resulted in a negative torque coefficient which was not physical.

At higher Reynolds numbers, i.e., Reynolds numbers greater than 1.0E+06 (which represents higher rotating speed in our experiment), all lines become flat and this means C_t becomes independent of Reynolds number.

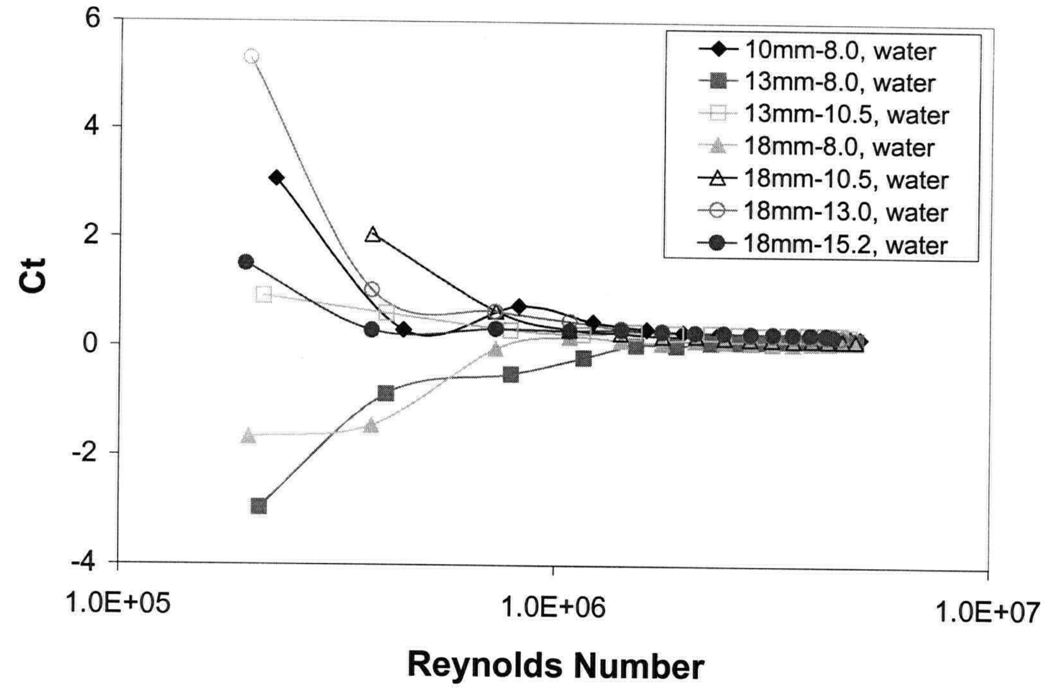

Figure 4.11: Ct Number vs. Reynolds Number for rotors with elements in water.

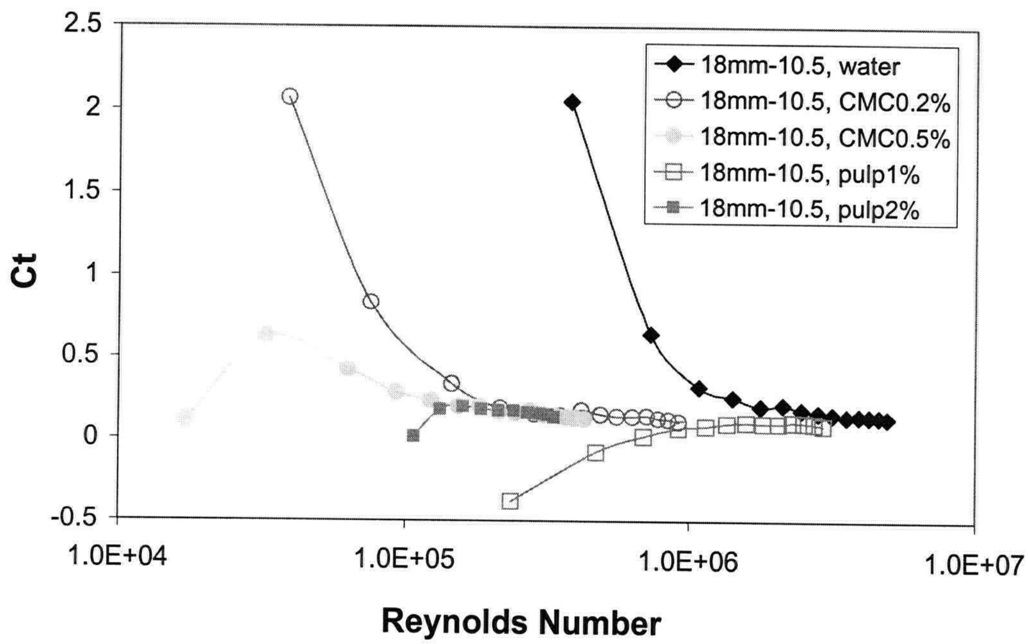

Figure 4.12: Ct vs. Re for constant elements height and constant spacing in different fluids. The spacing is 18mm, element height is 10.5mm.

When we turned to different fluids, the conclusion was also applicable. The torque coefficient for different fluids under the same outer conditions was shown in

Figure 4.12. It is apparent that different fluids with different viscosity have the same feature as that of water in Figure 4.11. When the Reynolds numbers were increasing, the C_t values became constant, though constant values were slightly different. Meanwhile, as all the C_t values for different fluid approximately aligned on one line, it indicated that different viscosities didn't make apparent difference to the torque coefficient in the state of fully turbulent flow.

4.3.3 Parameters affecting $C_{t\infty}$

From the previous dimensional analysis, we learned that C_t becomes independent at high Reynolds numbers. The value of the torque coefficient where it is independent of Reynolds number is called $C_{t\infty}$. These high Reynolds numbers are typical of industrial operating conditions; therefore, we are interested in understanding the effect of the element height, spacing and fluid type on $C_{t\infty}$.

4.3.3.1 Varying spacing, constant element height

The relationship between $C_{t\infty}$ and scaled spacing s/D (D is the diameter of the fixed outer cylinder) under constant element height was shown in Figure 4.13. $C_{t\infty}$ decreases as s/D increases. Since $g = s - h$, a decrease in spacing can be interpreted as downsizing of the gap when element height is constant. So the effect from varying spacing can be explained by the effect from the gap size. The smaller gap would strengthen the pressure stress in the leading edge of the element, and also generate more vortices downstream. Both of the two effects resulted in higher torque on the rotor under small spacing.

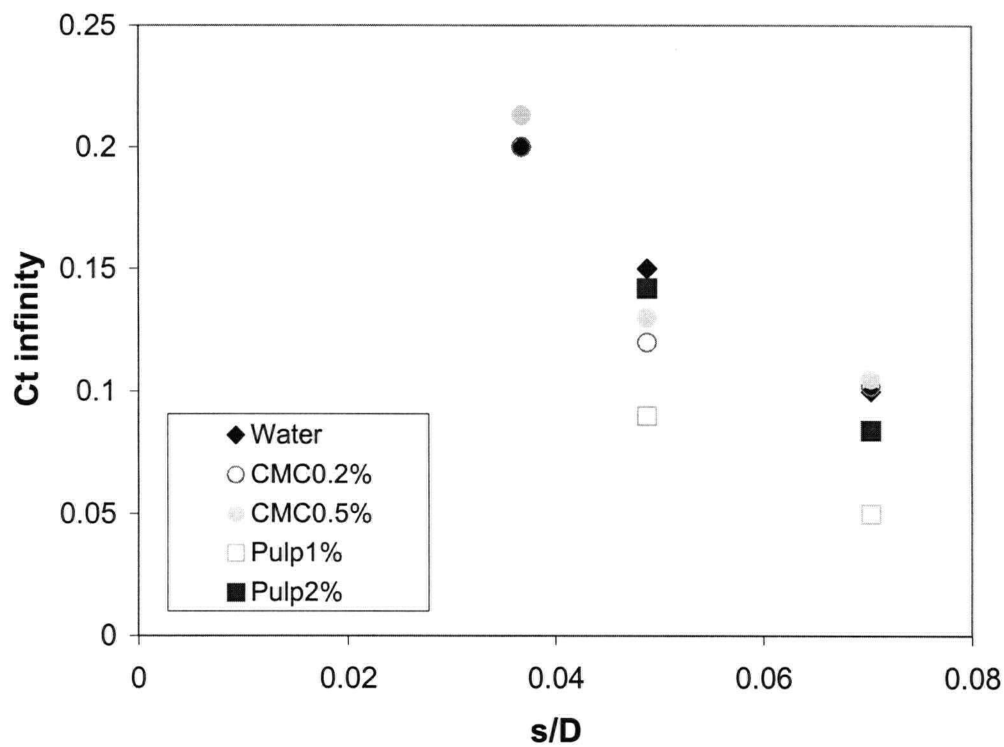

Figure 4.13: $C_{T\infty}$ **Number vs. s/D at constant element height of 8mm in different fluids.**

4.3.3.2 Varying elements, constant spacing

The plot of $C_{t\infty}$ with h/D was shown in Figure 4.14. It is evident that $C_{t\infty}$ increased quickly with the element height. This result confirmed the measurement that the element height had a great impact on the torque. However, the fluid viscosity didn't show any apparent influence on the value $C_{t\infty}$.

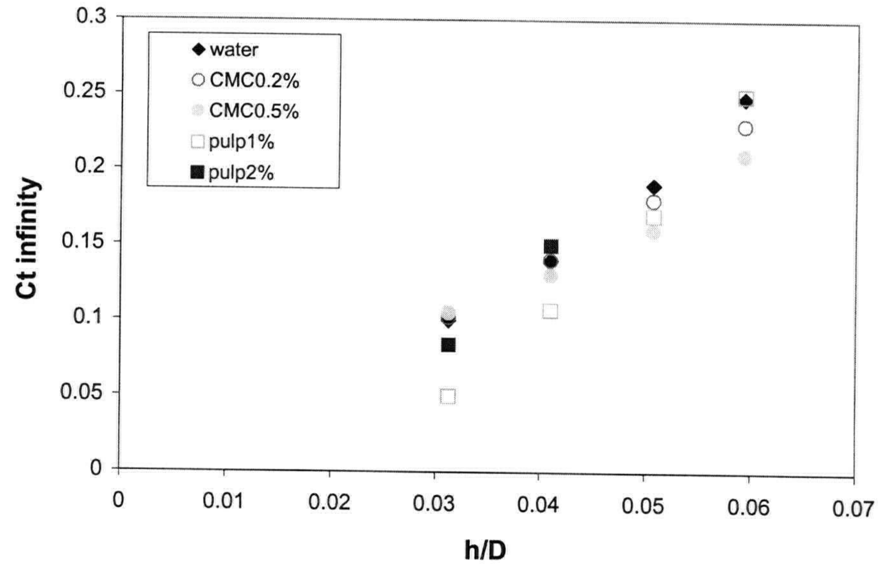

Figure 4.14: $C_{T\infty}$ vs. h/D for rotors with different element height running in different fluids. (Constant spacing is 18mm, heights varied from 8mm to 15.2mm).

4.3.3.3 Ratio of element height with spacing

Because both rotor spacing and element height have significant effects on the torque, we tried to explore the combined effect of these two parameters. Figure 4.15 illustrated $C_{t\infty}$ value at different h/s for water. It is clear that the relationship between $C_{t\infty}$ and h/s was nonlinear, and when the value of h/s approached zero, $C_{t\infty}$ reached zero, too. For other fluids, this conclusion was also applicable (shown in Figure 4.16), but the different viscosities didn't lead to much difference in $C_{t\infty}$ value.

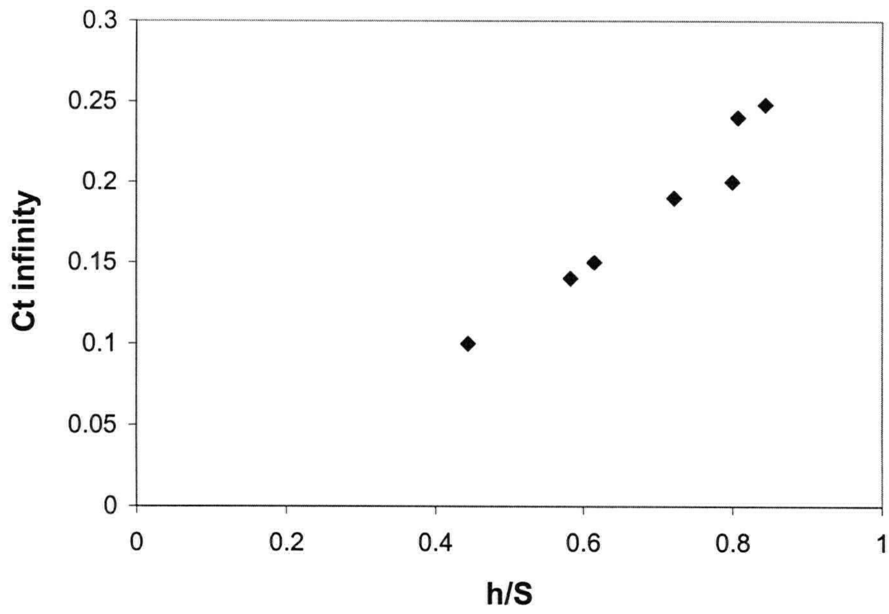

Figure 4.15: $C_{T\infty}$ **vs. H/S under varied spacing and element heights in water.**

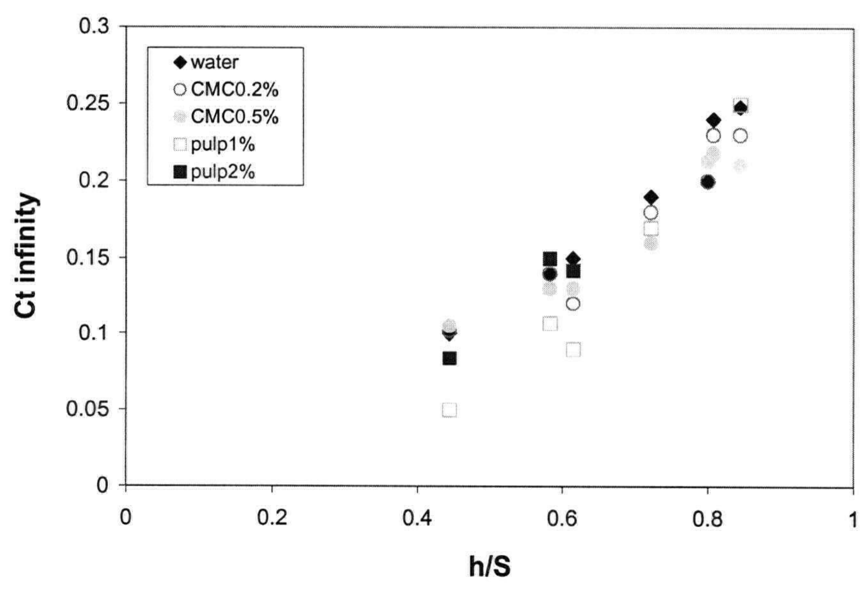

Figure 4.16: $C_{T\infty}$ **vs. h/S of rotors with elements running in CSS (different element height, different rotor spacing, and different fluids).**

4.3.4 Summary

In this section we have shown that the height and spacing of the elements significantly affect the torque (power) required by the rotor. We have also shown that at high Reynolds numbers the torque was independent of Reynolds number and indicates that the flow was fully turbulent. This was further confirmed by the fact that the torque coefficient was also independent of the fluid viscosity at high Reynolds numbers, which would be expected if it was truly Reynolds independent.

Chapter 5 Summary and conclusions

Pressure screens are an increasingly important unit operation in the manufacture of high quality pulp and paper. Reducing the power consumed by pressure screens can directly reduce the product cost. The objective of this study is to experimentally determine effect of the rotor design and operating variables on the power consumption using the Cross Sectional Screen (CSS), a laboratory screen designed to emulate a cross section of an industrial pressure screen. The experimental results are given in dimensionless form for application to industrial screens. The experimental results fall into two categories: smooth rotors (i.e., rotors without hydrodynamic elements) and rotors with elements.

Smooth rotors:

For all conditions tested, the measured torque (and power) increased with the rotating speed nonlinearly and the spacing between the rotor and the outer wall had relatively slight influence on the torque. The fluid viscosity, on the other hand, affected the flow behavior in different ways. CMC solutions had higher viscosity than water; consequently, they consumed more torque. However, since CMC solutions are a kind of shear shinning fluid, the toque-RPM curves were not as steep as that of water, i.e., the CMC curves crossed the water curve at high rotating speeds. In contrast, pulp suspensions with a higher viscosity than water, showed different features in torque-RPM curves. At low rotational speeds, the pulp suspensions required significantly more torque than water. It is hypothesized that the pulp was not entirely fluidized (not fully turbulent), i.e., the suspension exhibited partial plug flow due to the finite yield stress and low shear in some regions. When the rotational speed exceeded a certain value, the flow became fully turbulent, and the pulp suspensions generated less torque than that of water. This unusual phenomenon is called "drag reduction" in pulp suspension and is widely recognized in pipe flow.

Since the flow in CSS with a smooth rotor is similar to the Couette-Taylor flow, the same torque-scaling group $T_N = T/\rho v^2 L$ was employed in the non-dimensional analysis. The velocity was scaled as a Reynolds Number based on the rotor radius. For a concentric rotary device with relative high radius ratio, the non-dimensional toque measurements was independent of the geometry, and could be expressed as a power-law function of Reynolds Number only: $T_N \sim R_{e2}^{\alpha}$. The exponent α increased with the Reynolds number instead of being stable. In our experiments, α is between 1.32 and 1.68.

Rotors with elements:

Element height had significant influence on the torque in all the tested fluids. The additional torque resulted from the high normal pressure drag on the leading edge of the elements, and relatively low pressure in the region behind the elements where vortices and flow separation occurred. Based on this assumption, the additional torque generated by elements was scaled using the normal torque coefficient, C_t, modified for torque.

When plotted against Reynolds number, C_t became a constant at high Reynolds Numbers. This indicates that C_t is independent of Reynolds number in fully turbulent flow. The effect of the remaining experimental variables is expressed as changes in the constant, C_t, defined as $C_{t\infty}$ varied with the experimental condition.

The fluid viscosity didn't have significant effect on the additional torque for rotors with elements confirming the hypothesis that the flow is Reynolds independent at high Reynolds numbers. Furthermore, the "drag reduction" phenomena for pulp suspensions were not as apparent as that of smooth rotors. In 1% pulp suspension, the additional toque on the elements was slightly less than that in water under lower element height, but close or even over that in water when elements height getting higher. In 2% pulp suspensions, the torque was higher than that in water under the same operating conditions. According to our observation, this might result from the flocs accumulated in the front area of the elements when the ratio of element height over rotor spacing h/s is relatively large.

As mentioned above, $C_{t\infty}$ was independent of fluid viscosity, then, it can be approximately expressed as a function of the element height and the rotor spacing:

$$C_{t\infty} = f(h/D, s/D) \tag{5.1}$$

From experimental results, the data suggest that the key variable is a combination of these two variables, i.e., it is simply a function of ratio of element height with rotor spacing:

$$C_{t\infty} = f(h/s) \tag{5.2}$$

In summary, we have shown that the power required to turn a rotor has two parts: The power required to turn the central (smooth) core, which is a function of Reynolds number, and the additional power to move the hydrodynamic elements which is independent of Reynolds number but is a strong function of element height divided by spacing.

Bibliography

1. Corson S.R., Wakelin R.F., Loyd M.D. "TMP furnish development strategies, Part 1: Fractionation and long fibre removal". *Pulp and Paper Canada*, 97(12): 446-449 (1996).

2. Corson S.R., Wakelin R.F., Loyd M.D. "TMP furnish development strategies, Part 2: Sheet Properties". *Pulp and Paper Canada*, 98(1): 41-44 (1997).

3. Scott G.M., Abubarkr S. "Fractionation of secondary fibre - a review". *Progress in Paper Recycling* 3(3): 50-59.

4. Lapierre L., Pitre D., and Bouchard J. "Bleaching of deinked recycled pulp: benefits of fibre fractionation". *Pulp and Paper Report 1357,* 1998.

5. Gullichsen J., Greenwood B., Harkonen E., Ferritius O., and Tistad G. "Medium consistency technology: the MC screen". *TAPPI Journal*, 68(11): 54-58 (1985).

6. Irvine Jr. T.F., Capobianchi M. "Section 3: Non-Newtonian Flows". The CRC Handbook of Mechanical Engineering, CRC Press, Inc. pp 114-127(1998).

7. Bennington C.P.J., Kerekes R.J., Grace J.R. "Motion of Pulp Fibre Suspensions in Rotary Devices". *Can. J. Chem. Eng.* 69: 251-258 (1991)

8. Kerekes R.J., Soszynski R.M., Tam Doo P.A. "The Flocculation of Pulp Fibres". *Trans. Eighth Fund. Res. Symp., Mech. Eng. Pub. Ltd.*, Oxford, Vol. 1: 265-310 (1985).

9. Kerekes R.J. "Characterizing Fibre Suspensions". *TAPPI Engineering Conference Proceedings* (1996): 21-28

10. Kerekes R.J. "Pulp Floc Behavior in Entry Flow to Constrictions". *TAPPI Journal*, 66(1): 88-91 (1983).

11. Bennington C.P.J., Kerekes R.J., Grace J.R. "The Yield Stress of Fibre Suspensions". *Can. J. Chem. Eng.* 68: 748-757 (1990)

12. Chen K.F., Chen S.M. "The determination of the critical shear stress for fluidization of medium consistency suspensions of straw pulps". *Nordic Pulp and Paper Res. Journal* (1): 20-22 (1991).

13. Wikström T., Rasmuson A. "Yield Stress of Pulp Suspensions". *Nordic Pulp and Paper Res. Journal*, 13(3): 243-250 (1998).

14. Gullichsen J., Harkonen E. "Medium Consistency Technology I: Fundamental Data". *TAPPI Journal*, 64(6): 69-71 (1981).

15. Powell R.L., Weldon M., Ramaswamy S., McCarthy M.J. "Characterization of pulp suspensions". *TAPPI Engineering Conference Proceedings* (1996): 525-533

16. Swerin A., Powell R.L., Odberg L. "Linear and Nonlinear Dynamic Viscoelasticity of Pulp Fiber Suspensions". *Nordic Pulp and Paper Res. Journal*, no.3: 126-132 (1992).

17. Wiström T. "Flow and rheology of pulp suspensions at medium consistency". PhD thesis, Chalmers University of Technology, Sweden (2002).

18. Harkonen E.J. "Variables influencing the power consumption in medium consistency mixing". *TAPPI Medium Consistency Mixing Seminar Notes.* (1985): 45-49

19. Duffy G.G. "Flow of medium consistency wood pulp fibre suspensions". *Appita J.* 48(1): 51-55 (1995).

20. Wahren D. "Fibre network structures in papermaking operations". *Processing of the Conference on Paper Science and Technology: The Cutting Edge*, Institute of Paper Chemistry, Atlanta, pp.: 112-132 (1980).

21. Bennington C.P.J., Kerekes R.J. "Power Requirements for Pulp Suspension Fluidization". *TAPPI Journal*, 79(2): 253-258 (1996).

22. Brecht W., Heller H., "A study of the pipe friction losses of paper stock suspensions". *TAPPI Journal*, 33(9): 14A-48A (1950).

23. Nikula S. "On development of mechanical pulp screening". *Paperi ja Puu – Paper and Timber* 5: 458-459 (1989).

24. Boettcher P.C. "Results from a new design of contoured screen plate". *TAPPI Pulping Conference Proceedings* (1986): 279-283.

25. Frejborg F., Giambrone J. "Improvements of new and old screens in cleaning efficiency at maintained or increased capacity". *TAPPI Pulping Conference Proceedings* (1989): 529-532

26. Hooper A.W., Pulp and Paper Manufacture, 3rd ed., Vol.5, The Screening of Chemical pulp, The Joint Textbook Committee of the Paper Industry, *Canadian Pulp and Paper Association*, Montreal, 1989.

27. Gooding R.W. "Flow resistance of screen plate apertures". PhD Thesis, University of British Columbia, Vancouver, BC, Canada (1996).

28. Halonen L., Ljokkio R., Peltonen K. "Improved screening concepts". *TAPPI Conference Proceedings*, Atlanta (1990): 207-212

29. Yu C.J., Defoe R.J. "Fundamental study of screening hydraulics. Part 1: Flow patterns at the feed-side surface of screen baskets; mechanism of fiber-mat formation and remixing". *TAPPI Journal*, 77(8): 219-226 (1994).

30. Yu C.J., Defoe R.J. "Fundamental study of screening hydraulics. Part 2: Fiber orientation in the feed side of a screen basket". *TAPPI Journal*, 77(9): 119-124 (1994).

31. Yu C.J., Crossley B.R. "Fundamental study of screening hydraulics. Part 3: Model for calculating effective open area". *TAPPI Journa*l, 77(9): 125-131 (1994).

32. Koffinke R.A., Benedict J.E. "Modern screening developments". *TAPPI Pulping Conference Proceedings* (1984): 539-541.

33. McCarthy C. "Factors affecting Pressure Screen Capacity". *TAPPI Engineering Conference Proceedings* (1987): 355-361

34. Gooding R.W., Kerekes R.J. "Consistency changes caused by pulp screening". *TAPPI Journal*, 75(11): 109-118 (1992).

35. Kumar A., Gooding R.W., and Kerekes R.J. "Factors controlling the passage of fibers through slots". *TAPPI Journal*, 81(5): 247-254 (1998).

36. Karvinen R., Halonen L. "The effect of various factors on pressure pulsation of a screen". *Paperi ja Puu* 66(2): 80-83 (1984).

37. Goldenberg P.H. "Recent developments in screening". *TAPPI Pulping Conference Proceedings* (1989): 73-75.

38. Clement L., Pikka O. "New screening concept generates superior screening efficiency". *Paperi ja Puu – Paper and Timber* 73(6): 508-511 (1991).

39. Niinimaki J., Dahl O., Hautala J., Tirri T., and Kuopanportti H. "Effect of operating parameters and rotor body shape on flow conditions and the

performance of a pressure screen". *TAPPI Pulping Conference Proceedings* (1996): 761-766.

40. Oosthuizen P.H., Chen S., Kuhn D.C.S., Whiting P. "Fluid and fibre flow near a wall slot in a channel". *78th Annual Meeting Proceedings, Tech. Sect., CPPA,* Montreal (1992): B49-52

41. Gooding R.W., Kerekes R.J. "The motion of fibres near a screen slot". *JPPS* 15(2):59-62 (1989).

42. Gooding R.W. "The Passage of fibres through slots in pulp screening". M.A.Sc. Thesis, University of British Columbia, Vancouver, BC, Canada (1986).

43. Gonzalez J.A. "Characterization of design parameters for a free foil rotor in a pressure screen". M.A.Sc. Thesis. Dept. Mechanical Engineering, University of British Columbia (2002).

44. Feng M. "Numerical simulations of pressure pulses produced by a pressure screen foiled rotor". M.A.Sc. Thesis. Dept. Mechanical Engineering, University of British Columbia (2003).

45. Wakelin R.F., Corson S.R. "TMP long fibre fractionation with pressure screens". *Proceedings of the 1995 International Mechanical Pulping Conference, Ottawa* (1995): 257-265.

46. Olson J.A., Roberts N., Allison B.J., and Gooding R.W. "Fibre length fractionation caused by pulp screening". *JPPS* 24(12): 393-397 (1998).

47. Allison B.J., Olson J.A. "Optimization of multiple screening stages for fibre length fractionation: two stages case". *JPPS* 26(3): 113-119 (2000).

48. Kumar A. "Passage of fibres through screen apertures". Ph.D. thesis, University of British Columbia, Vancouver, BC, Canada (1991).

49. Olson J.A. "The effect of fibre length on passage through narrow apertures". PhD Thesis. Dept. Chem. Eng., University of British Columbia (1996).

50. Olson J.A., Kerekes R.J. "Fibre passage through a single screen aperture". *Appita J.* 51(2): 122-126 (1998).

51. Olson J.A., Wherrett G. "A model of fibre fractionation by slotted screen apertures". *JPPS* 24(12): 398-403 (1998).

52. Olson J.A., Allison B.J., and Roberts N. "Fibre length fractionation caused by pulp screening. Smooth-hole screen plates". *JPPS* 26(1): 12-16 (2000).

53. Ammala A., Dahl O., Kuopanportte H., Niinimaki J. "Pressure screening: changes in pulp properties in the screen basket". *TAPPI Journal*, 82(10): 99-104 (1999).

54. Repo K, Sundholm J. "The effect of rotor speed on the separation of coarse fibres in pressure screening with narrow slots". *Pulp & Paper Canada J.* 97(7): 67-71 (1996).

55. Ammala A., Jussila T., Niinimaki J. "On the explanatory nature of reject rates for the fractionation of pulp with slotted pressure screens". *Paperi ja Puu – Paper and Timber* 83(2): 128-131 (2001).

56. Nelson G.L. "The screening quotient: a better index of screen performance". *TAPPI Journal*, 64(5): 133-134 (1981).

57. Fredriksson B. "Evaluation of apparatus and systems for screening mechanical pulp". *Svensk Papperstidn* (12): R94-98 (1984)

58. Nguyen K.L., Eagle A.J., van Klaveren M.E. "Analysis and optimization of a pulp screening system". *Appita J.* 44(5): 337-338 (1991).

59. Wakelin R.F. "Prediction of fractionation efficiency for pressure screens". *Appita J.* 50(4): 295-300 (1997).

60. Sloane C.M. "Kraft pulp processing – pressure screen fractionation". *Appita J.* 53(3): 220-226 (2000).

61. Heise O. "Slotted headbox screening for fine, publication, and newsprint grades". *TAPPI Journal*, 78(2): 117-119 (1992).

62. Levis S. "Removal of contaminants from recycled fiber high/low density screening". *Recycling and Deinking of Newsprint and Fine Papers Course Notes,* CPPA, Montreal, 1991.

63. Vitori C.M. "Stock velocity and stickies removal efficiency in slotted pressure screens". *1991 recycling Forum*, CPPA, Toronto, p.133.

64. Niinimaki J., Dahl O., Kuopanportti H., and Ammala A. "A comparison of pressure screen baskets with different slot widths and profile heights". *Paperi ja Puu – Paper and Timber* 80(8): 601-605 (1998).

65. Martinez D.M., Gooding R.W., Roberts N. "A force balance model of pulp screen capacity". *TAPPI Journal*, 82(4): 181-187 (1999).

66. Gooding R.W., Craig D.F. "The effect of slot spacing on pulp screen capacity". *TAPPI Journal*, 75(2): 71-75 (1992).

67. Niinimaki J., Dahl O., Hautala J., and Kuopanportti H. "Effect of the pressure difference over the screen basket on the performance of a pressure screen". *TAPPI Journal*, 82(4): 176-180 (1999).

68. Wakelin R.F., Blackwell B.G., Corson S.R. "The influence of equipment and process variables on mechanical pulp fractionation in pressure screens". *Proc. 48th Appita Annual Conference, Melbourne* (1994): 611-615

69. Wahren D. "Fundamentals of suspension screening". *Svensk Papperstidn* 82(18): 539-546(1979).

70. Lawryshyn Y.A., Kuhn D.C.S. "Simulation of flexible fibre motion through screen apertures". *JPPS* 24(12): 404-411 (1998).

71. Coles D. "Transition in circular Couette flow". *J. Fluid Mech.* 21: 385-425 (1965)

72. Gollub J. P., Swinney H. L., "Onset of turbulence in rotating a fluid". *Physics Review Letters* 35: 927-930 (1975).

73. Fenstermacher P.R., Swinney H.L. "Dynamical instabilities and the transition to chaotic Taylor vortex flow". *J. Fluid Mech.* 94: 103-128 (1979)

74. Brandstater A., Swinney H.L., "Strange attractors in weakly turbulent Couette-Taylor flow". *Physics Review A35*: 2207-2220 (1987).

75. Wendt F. Ingenieur-Archiv. 4, 577 (1933)

76. Taylor G.I., Philos. Trans. R. Soc. London A 223, 289 (1923)

77. Tong P., Goldburg W.I., Huang J.S., Witten T.A."Anisotropy in turbulence drag reduction". *Physics Review Letters* 65: 2780-2783 (1990).

78. Marcus P.S. "Simulation of Taylor-Couette flow. Part 2. Numberical results for wavy-vortex flow with one traveling wave". *J. Fluid Mech.* 146: 65-113 (1984)

79. Barcilon A., Brindley J., "Organized structures in turbulent Taylor-Couette flow". *J. Fluid Mech.* 143: 429-449 (1984)

80. Couette M.M., Ann. Chim. Phys. Ser. VI 21, 433 (1890).

81. Nickerson E.C., "Upper bounds on the torque in cylindrical Couette flow". *J. Fluid Mech.* 38: 807-815 (1969)

82. Doering C.R., Constantin P., "Energy dissipation in shear driven turbulence". *Physics Review Letters* 69: 1648-1651 (1992).

83. Lathrop D.P., Fineberg J., Swinney H.L. "Transition to shear-driven turbulence in Couette-Taylor flow". *Physics Review A46*: 6390-6405 (1992).

84. Lathrop D.P., Fineberg J., Swinney H.L. "Turbulent flow between concentric rotating cylinders at large Reynolds number". *Physics Review Letters* 68: 1515-1518 (1992).

85. Lewis G. S., Swinney H. L., "Velocity structure functions, scaling, and transitions in high-Reynolds number Couette-Taylor flow". *Physics Review E 59(5):* 5457-5467 (1999).

86. Webpage of Binsfeld Engineering Inc.: http://www.binsfeld.com/techinfo.cfm